



## Original article

## Impact of FASN-enriched EVs on endothelial cell function in obstructive sleep apnea hypopnea syndrome

Yuan Tian <sup>a,1</sup>, Dan Zhang <sup>b,1</sup>, Huaian Yang <sup>c</sup>, Xiaoli Zhang <sup>d,\*\*</sup>, Shengqun Xu <sup>c,\*</sup><sup>a</sup> Department of Otolaryngology Head and Neck Surgery, Shengjing Hospital of China Medical University, Shenyang 110004, China<sup>b</sup> Department of Pediatrics, Shengjing Hospital of China Medical University, No. 36, Sanhao Street, Heping District, Shenyang, 110004, China<sup>c</sup> Ear, Nose, Throat, Head and Neck Surgery Comprehensive Ward, Shengjing Hospital of China Medical University, Shenyang 110020, China<sup>d</sup> Department of Critical Care Medicine, Shengjing Hospital of China Medical University, No. 36, Sanhao Street, Heping District, Shenyang, 110004, China

## ARTICLE INFO

## Article history:

Received 31 July 2024

Received in revised form

11 February 2025

Accepted 27 February 2025

Available online 1 March 2025

## Keywords:

Obstructive sleep apnea hypopnea syndrome

Extracellular vesicles

Fatty acid synthase

Fatty acid metabolism

Proteomics

## ABSTRACT

Endothelial dysfunction is a key factor linking obstructive sleep apnea hypopnea syndrome (OSAHS) with cardiovascular diseases. In this study, we used advanced proteomics and metabolomics approaches to investigate the impact of extracellular vesicles (EVs) derived from the serum of OSAHS patients on endothelial function. Our multi-omics analysis identified dysregulated pathways related to fatty acid metabolism, apoptosis regulation, and inflammatory responses, highlighting fatty acid synthase (FASN) as a crucial player in OSAHS-induced endothelial dysfunction. Both *in vitro* and *in vivo* experiments demonstrated that FASN-enriched EVs impair endothelial cell viability and disrupt metabolic homeostasis, offering new insights for the development of targeted therapies for cardiovascular complications associated with OSAHS.

© 2025 The Authors. Published by Elsevier B.V. on behalf of Xi'an Jiaotong University. This is an open access article under the CC BY-NC-ND license (<http://creativecommons.org/licenses/by-nc-nd/4.0/>).

## 1. Introduction

Obstructive sleep apnea hypopnea syndrome (OSAHS) is a severe sleep disorder characterized by intermittent hypoxia and fragmented sleep, which predisposes patients to a range of clinical complications including chronic inflammation, reduced sleep quality, and heightened cardiovascular risk [1]. These symptoms significantly increase the disease burden and complicate clinical management for OSAHS patients. By conducting in-depth analysis on clinical samples, we aim to uncover the physiological and pathological mechanisms underlying OSAHS and its related complications, thereby providing a foundation for more precise and individualized diagnostic and therapeutic strategies [2,3].

OSAHS patients frequently experience chronic intermittent hypoxia (CIH) and fragmented sleep, both of which contribute to cardiovascular disease [4–6]. Endothelial dysfunction is widely recognized as a key pathological mechanism through which OSAHS promotes cardiovascular complications [7–9].

While research on OSAHS has mainly focused on its clinical manifestations and treatment, fewer studies have delved into the underlying molecular mechanisms. In particular, the biological pathways through which OSAHS influences the cardiovascular system are not yet fully understood. Our study identifies a positive correlation between C-reactive protein (CRP) levels and OSAHS, as indicated by the apnea-hypopnea index (AHI), with elevated CRP levels often signaling the presence of inflammation. Additionally, extracellular vesicles (EVs) have garnered attention in recent years as crucial mediators of intercellular communication. These EVs, which carry bioactive molecules such as proteins, lipids, and RNA, play significant roles in numerous physiological and pathological processes [10–12].

A prominent feature of OSAHS is intermittent hypoxia caused by breathing pauses [13], which triggers specific changes in plasma EVs. Direct contact between serum-derived EVs (s-EVs) and the vascular endothelium leads to cardiovascular damage [14–16]. Investigating the protein composition of EVs in the serum of OSAHS

Peer review under responsibility of Xi'an Jiaotong University.

\* Corresponding author.

\*\* Corresponding author.

E-mail addresses: [zhangxl1@sj-hospital.org](mailto:zhangxl1@sj-hospital.org) (X. Zhang), [xusq@sj-hospital.org](mailto:xusq@sj-hospital.org) (S. Xu).

<sup>1</sup> These authors contributed equally to this work.

<https://doi.org/10.1016/j.jpaha.2025.101251>

2095-1779/© 2025 The Authors. Published by Elsevier B.V. on behalf of Xi'an Jiaotong University. This is an open access article under the CC BY-NC-ND license (<http://creativecommons.org/licenses/by-nc-nd/4.0/>).

patients can help elucidate their role in the disease's pathogenesis, offering new biomarkers for early diagnosis, treatment, and prognosis. Additionally, such research can improve our understanding of intercellular communication, allowing for the development of more precise and effective treatment approaches for OSAHS patients.

In this study, we employed proteomics and metabolomics to conduct a detailed analysis of EVs in the serum of OSAHS patients, focusing on their specific role in endothelial dysfunction. By comparing the protein and metabolite composition of EVs from OSAHS patients and healthy individuals, we aim to reveal the pathophysiological changes associated with OSAHS. Fatty acid synthase (FASN), a key enzyme in fatty acid metabolism, has been implicated in various metabolic disorders [17,18]. Elevated FASN expression has been observed in cardiovascular diseases, including coronary atherosclerosis [19]. FASN is also involved in endothelial cell lipid metabolism and nitric oxide synthase (NOS) activity [20]. Inhibiting FASN has been shown to improve endothelial function, reduce inflammation, and alleviate oxidative stress [21]. Our preliminary research suggests that FASN expression is upregulated in EVs from OSAHS patients, indicating its potential role in OSAHS-induced endothelial dysfunction.

This study aims to clarify the role of FASN-enriched EVs in OSAHS-related endothelial dysfunction, offering new insights into the pathogenesis of this complex disease. These findings not only deepen our understanding of the relationship between OSAHS and cardiovascular diseases but also provide essential data to support the development of targeted therapeutic strategies. Such molecular-level research offers the potential for more precise and effective approaches in future clinical studies and treatments, ultimately improving the prognosis and quality of life for OSAHS patients.

## 2. Materials and methods

### 2.1. Clinical sample collection

The study enrolled 76 patients from June 2020 to June 2021. These patients had undergone polysomnogram (PSG) examinations in the past year, with their bed partners reporting symptoms such as fatigue, insomnia, snoring, and respiratory interruptions during sleep. OSAHS diagnosis was confirmed based on the AHI criteria  $\geq 5$ . Sleep quality deterioration, chronic inflammation, and increased cardiovascular disease risk were noted, although not all chronic inflammation and cardiovascular diseases were caused by OSAHS. To match the control group on age, body mass index (BMI), and other parameters, and reduce confounding variables, we excluded 36 patients with systemic hypertension, pulmonary hypertension, heart failure, myocardial ischemia/infarction, arrhythmias, cerebrovascular diseases or family history of cardiovascular diseases, diabetes, chronic obstructive and/or restrictive pulmonary diseases, hyperlipidemia, chronic liver failure, end-stage renal disease, inflammatory bowel disease, and similar conditions. We included 20 patients with AHI  $<5$  as the control group and 20 patients with AHI  $\geq 5$  as the OSAHS group. Blood samples (3–5 mL) were collected via antecubital vein puncture at 06:30, following overnight fasting and polysomnographic monitoring. All patients had their height, weight, general physical examination, systolic and diastolic blood pressure, and blood and biochemical analyses. The study protocol was approved by the Clinical Ethics Committee of Shengjing Hospital of China Medical University (Approval No.: 2024PS160K) and patients provided informed consent according to the Helsinki Declaration. Detailed clinical information is available in [Table S1](#).

### 2.2. Isolation, identification, and quantification of s-EVs

Serum samples were processed through sequential centrifugation steps: 3,000 g for 15 min, 2,000 g for 15 min, and 10,000g for 20 min. After filtration with a 0.22  $\mu\text{m}$  filter, samples were ultracentrifuged at 110,000 g for 70 min at 4  $^{\circ}\text{C}$ , resuspended in phosphate-buffered saline (PBS), and subjected to a second ultracentrifugation step. The final pellet was resuspended in 100  $\mu\text{L}$  of sterile PBS for subsequent experiments. Ultracentrifugation was performed using a Beckman Optima L-90K ultracentrifuge with an SW-32Ti rotor (Beckman Coulter, Brea, CA, USA).

Western blot analysis confirmed the presence of s-EV surface markers heat shock protein 70 (HSP70), cluster of differentiation 9 (CD9), CD81 and the absence of albumin (negative control). s-EVs were visualized using transmission electron microscopy (TEM), with 20  $\mu\text{L}$  of s-EV suspension applied to a copper grid, stained with phosphotungstic acid, and imaged using a Hitachi H-7650 electron microscope (Hitachi High-Technologies Corporation, Tokyo, Japan). The particle size and concentration of s-EVs were measured via nanoparticle tracking analysis (NTA), and protein content was determined using a bicinchoninic acid (BCA) assay.

### 2.3. Animal experiment

All animal procedures adhered to the NIH Guide for the Care and Use of Laboratory Animals and were approved by the Animal Ethics Committee of Shengjing Hospital of China Medical University (Approval No.: 2024PS374K). Male BALB/c mice (8–10 weeks old, 23–27 g) were randomly assigned to either CIH or normoxia (NO) conditions. Mice were exposed to CIH (8 h/day) consisting of alternating 30-s cycles of hypoxia (5%  $\text{FiO}_2$ ) and NO (21%  $\text{FiO}_2$ ) for 14 days, while NO mice were exposed to normal air to account for environmental differences.

For the first experiment, the mice were divided into the following groups: 1) NO Ctrl: normoxia, injected with PBS; 2) NO + Ctrl s-EVs: normoxia, injected with healthy donor s-EVs; 3) NO + OSAHS s-EVs: normoxia, injected with OSAHS patient s-EVs; 4) CIH: intermittent hypoxia, injected with PBS; 5) CIH + Ctrl s-EVs: intermittent hypoxia, injected with healthy donor s-EVs; and 6) CIH + OSAHS s-EVs: intermittent hypoxia, injected with OSAHS patient s-EVs. s-EVs were administered for one week, and mice were sacrificed on day 15 for tissue and blood analysis. *In vivo* tracking of s-EVs was performed using PKH26 fluorescent dye labeling.

In the second experiment, gene intervention was performed to assess the effect of FASN on endothelial dysfunction. The groups included: 1) NO: normoxia, injected with PBS; 2) CIH: intermittent hypoxia, injected with PBS; 3) CIH + sh-NC: intermittent hypoxia, injected with control shRNA (sh-NC); and 4) CIH + sh-FASN: intermittent hypoxia, injected with FASN-targeting shRNA (sh-FASN). On day 15, blood was collected to extract EVs for cell experiments, and tissues were harvested post-euthanasia for subsequent analysis.

For lentiviral transduction, mouse-derived FASN-shRNA sequences targeting FASN were designed as follows: sh-FASN-1 (5'-3': GCTGGTCGTTTCTCCATTA) and sh-FASN-2 (5'-3': CCCTTGATGAAGAGGGATCAT). A non-targeting control shRNA (sh-NC; 5'-3': CCTAAGGTTAAGTCGCCCTCG) was used as a negative control. All shRNA constructs were obtained from Thermo Fisher (Waltham, MA, USA). HEK293T cells (catalog number: BFN60810479, ATCC, Manassas, VA, USA) were cultured in Dulbecco's modified Eagle medium (DMEM) supplemented with 10% fetal bovine serum (FBS; Gibco, Grand Island, NY, USA) at 37  $^{\circ}\text{C}$  in a 5%  $\text{CO}_2$  cell culture incubator. After 20 h, the medium was replaced with 12 mL of medium containing 5% FBS. Approximately 48 h later, the virus-

containing supernatant was collected, filtered through a 0.45  $\mu\text{m}$  cellulose acetate filter (HAWG04700, MF-Millipore, Billerica, MA, USA), and stored at  $-80\text{ }^{\circ}\text{C}$ . The cell line transfected with FASN-shRNA was designated as sh-FASN, while the control cell line was designated as sh-NC.

#### 2.4. Histology of lung tissue and lung injury score

The left upper lung lobes of mice treated with different EVs and under varying conditions were fixed in 4% paraformaldehyde for 24 h, embedded in paraffin, sectioned, and deparaffinized using xylene. Sections were dehydrated in a graded ethanol series (100%, 95%, and 70%) before being stained with hematoxylin (H8070, Solarbio, Beijing, China) for 5–10 min at room temperature. After rinsing with distilled water, the sections were dehydrated in 95% ethanol and stained with eosin (G1100, Solarbio) for 5–10 min, followed by standard dehydration, clearing and mounting. Lung injury was assessed based on parameters such as hemorrhage, congestion, alveolar wall edema, and inflammatory cell infiltration.

#### 2.5. Assessment of pulmonary vascular leak

Pulmonary vascular leakage was assessed using Evan's blue dye (EBD; E2129, Macklin, Shanghai, China). Mice were injected with 20 mg/kg of EBD via the tail vein and allowed a circulation time of 3 h. Anticoagulated blood was collected and centrifuged at 3,000 rpm for 20 min. The pulmonary vasculature was flushed with saline through the right ventricle for 5 min to remove excess dye. Lung tissues were then incubated in formamide (344206-M, Macklin, Shanghai, China) at  $60\text{ }^{\circ}\text{C}$  for 24 h to extract EBD. After centrifugation at 5,000 rpm for 30 min, the absorbance of the plasma and lung supernatant was measured at 620 nm using a spectrophotometry. The Evans blue leak index was calculated as the ratio of dye concentration in the lungs to that in the plasma.

#### 2.6. Measurement of endothelial cell permeability

For evaluate endothelial cell permeability, endothelial cells were cultured on collagen-coated polyester membrane Transwells (0.4  $\mu\text{m}$  pore size; Solarbio). After 48 h of co-incubation with s-EVs, 1 mg/mL fluorescein isothiocyanate (FITC)-dextran was added to the upper chamber. The fluorescence intensity of the medium in the lower chamber was measured using a BioTek Synergy H1 (BioTek, Winooski, VT, USA) 30 min after FITC-dextran stimulation. Dextran flux was calculated as the percentage of diffusion per square centimeter per hour.

#### 2.7. Transepithelial electrical resistance (TEER)

To assess endothelial barrier integrity, TEER was measured using a Millicell-ERS (MERS00002, Millipore, Billerica, MA, USA). Endothelial cells were grown to confluence on polycarbonate membranes in Transwells (0.4  $\mu\text{m}$  pore size; Solarbio). After co-incubation with s-EVs for 48 h, the TEER of the endothelial monolayer was measured at the tip of the electrodes in the upper and lower compartments and expressed in  $\Omega \cdot \text{cm}^2$ .

#### 2.8. Real-time quantitative reverse transcription polymerase chain reaction (RT-qPCR)

Total RNA was extracted from cells using the Trizol reagent kit (10296010, Thermo Fisher). The quality and concentration of the extracted RNA were evaluated using a Nanodrop UV-Vis spectrophotometry (ND-1000, Thermo Fisher). Reverse transcription was performed using the PrimeScript<sup>™</sup> RT-qPCR kit (RR086A, Takara

Bio Inc., Mountain View, CA, USA). RT-qPCR was carried out using SYBR Premix Ex Taq<sup>™</sup> (DRR820A, Takara Bio Inc.) on a LightCycler 480 system (Roche Diagnostics, Pleasanton, CA, USA). Glyceraldehyde-3-phosphate dehydrogenase (GAPDH) was used as the reference gene for mRNA quantification. Primer sequences for amplification were designed and provided by Shanghai General Biotechnology Co., Ltd. (Shanghai, China), as shown in Table S2. The formula for calculating the relative expression of the target gene in the experimental group compared to the control group was  $2^{-\Delta\Delta\text{Ct}}$ , with  $\Delta\Delta\text{Ct} = \Delta\text{Ct experimental group} - \Delta\text{Ct control group}$ , where  $\Delta\text{Ct} = \text{Ct target gene} - \text{Ct reference gene}$ .

#### 2.9. Immunofluorescence staining

##### 2.9.1. Cytochrome (Cyt c)

Samples were permeabilized with 0.1% Triton X-100 at  $4\text{ }^{\circ}\text{C}$  for 30 min, followed by three washes with PBS. Primary antibody Cyt-c (ab133504, Rabbit monoclonal, 1:250, Abcam, Cambridge, UK) was added and incubated overnight at  $4\text{ }^{\circ}\text{C}$ . After three washes with TBS containing 1% Tween-20 (TBST), the samples were incubated with the appropriate secondary antibody conjugated with Alexa Fluor 555/488 (Thermo Fisher) for 2 h at room temperature.

##### 2.9.2. CD31/ $\alpha$ -smooth muscle actin ( $\alpha$ -SMA)

Cells were fixed with 4% paraformaldehyde (30525-89-4, Sigma Aldrich, Shanghai, China) for 20 min, permeabilized with 0.5% Triton X-100 (9036-19-5, Sigma Aldrich) for 30 min, and blocked with 2% bovine serum albumin (BSA) for 1 h. Afterward, cells were incubated overnight at  $4\text{ }^{\circ}\text{C}$  with anti-CD31 (ab307336, Rabbit monoclonal, 1:100, Abcam) conjugated with Alexa Fluor 594. After washing with PBS, cells were incubated with anti- $\alpha$ -SMA (ab307770, 1:100, Abcam) conjugated with Alexa Fluor 488 overnight at  $4\text{ }^{\circ}\text{C}$ . After three TBST washes, cells were incubated with the secondary antibody conjugated with Alexa Fluor 555/488 for 2 h at room temperature.

##### 2.9.3. Terminal deoxynucleotidyl transferase dUTP nick end labeling (TUNEL)/CD31

Cells were treated with proteinase K and 3% hydrogen peroxide, followed by incubation with the TUNEL reaction mixture at  $37\text{ }^{\circ}\text{C}$  in a humid chamber. After rinsing with PBS, cells were incubated overnight at  $4\text{ }^{\circ}\text{C}$  with anti-CD31 conjugated with Alexa Fluor 488 (ab307133, 1:100, Abcam). After three washes with TBST, the secondary antibody was added and incubated for 2 h at room temperature. 4',6-diamidino-2-phenylindole (DAPI; D1306, Thermo Fisher) solution was then used for nuclear staining, and samples were analyzed under a fluorescence microscope.

##### 2.9.4. Intercellular adhesion molecule-1 (ICAM-1)/CD31

Cells were fixed with 4% paraformaldehyde for 20 min, permeabilized with 0.5% Triton X-100 for 30 min, blocked with 2% BSA for 1 h, and incubated overnight at  $4\text{ }^{\circ}\text{C}$  with anti-CD31 conjugated with Alexa Fluor 488 (ab307133, 1:100, Abcam). After washing with PBS, cells were incubated overnight at  $4\text{ }^{\circ}\text{C}$  with anti-ICAM-1 conjugated with Alexa Fluor 647 (ab214944, 1:100, Abcam). Following PBS washes, cells were incubated with the secondary antibody conjugated with Alexa Fluor 555/594 (Thermo Fisher) for 2 h at room temperature, followed by three washes with TBST.

##### 2.9.5. Interleukin-6 (IL-6)/ $\alpha$ -smooth muscle actin ( $\alpha$ -SMA)/F4/80

Paraffin sections were blocked with serum at room temperature for 1 h, then incubated overnight at  $4\text{ }^{\circ}\text{C}$  with anti-IL-6 conjugated with Alexa Fluor 488 (ab314590, Abcam). After washing with PBS, cells were incubated overnight at  $4\text{ }^{\circ}\text{C}$  with anti- $\alpha$ -SMA conjugated

with Alexa Fluor 647 (ab307771, 1:100, Abcam). A third antibody, PerCP/Cy5.5®-conjugated anti-F4/80 (ab210252, 1:100, Abcam), was added and incubated overnight at 4 °C. After PBS washes, cells were incubated with the secondary antibody conjugated with Alexa Fluor 555/594 for 2 h at room temperature, followed by three TBST washes.

After all staining procedures, DAPI (D1306, Thermo Fisher) solution was applied for nuclear staining. Cell images were captured using laser confocal microscopy with excitation wavelengths of 488 and 594 nm. Quantitative analysis was performed using ImageJ software, and total antibody staining was normalized to DAPI.

### 2.10. Isobaric tags for relative and absolute quantification (iTRAQ) labeling combined with mass spectrometry analysis

EVs from different groups were selected, and proteins were extracted using SDT lysis buffer (ED-8452, ECOTOP, Guangzhou, China). Protein quantification was performed using the BCA method (23227, Thermo Fisher). Thirty microliters of each protein sample were digested using the filter-aided sample preparation (FASP) method. Peptide segments were desalted with a C<sub>18</sub> cartridge (WAT051910, Waters Corporation, Milford, MA, USA) and concentrated by vacuum centrifugation. The dried peptides were resuspended in 40 µL of resolubilization buffer (GS1422, Beijing Biolab Sciences Co., Ltd., Beijing, China) and measured at 280 nm. One hundred micrograms of peptides from each sample were labeled according to the iTRAQ labeling kit protocol (4352135, Sigma Aldrich). The iTRAQ-labeled peptides were fractionated by strong cation exchange (SCX) chromatography on an AKTA Purifier 100 system (GE, Uppsala, Sweden) using reagent A (10 mM KH<sub>2</sub>PO<sub>4</sub>, 25% acetonitrile, pH 3.0) and reagent B (500 mM KCl, 10 mM KH<sub>2</sub>PO<sub>4</sub>, 25% acetonitrile, pH 3.0), followed by desalting with a C<sub>18</sub> cartridge after freeze-drying. Peptide separation was performed using a nanoflow high-performance liquid chromatography (HPLC) system (Alliance HPLC, Waters Corporation) and Easy nLC. Buffer A was 0.1% formic acid in water, and buffer B was 0.1% formic acid in 84% acetonitrile. After equilibrating the chromatographic column with buffer A, samples were loaded onto a trap column (nanoViper C18, Thermo Fisher) and separated on an analytical column (C18-A2, Thermo Fisher) at a flow rate of 300 nL/min. The separated peptides were analyzed by a Q Exactive Orbitrap mass spectrometer (Thermo Fisher).

### 2.11. Protein database search and data processing

Liquid chromatography-mass spectrometry/mass spectrometry (LC-MS/MS) data were processed and analyzed using MaxQuant software (v1.5.2.8) for peptide identification and protein quantification. Searches were performed against the UniProt 14.1 (2009, Cambridge, UK; Washington, DC, USA; Hinxton, UK) *Gossypium hirsutum* and reverse decoy databases. Trypsin/P was selected as the cleavage enzyme, allowing up to two missed cleavages. The initial search tolerance was set to 20 ppm, the main search tolerance to 5 ppm, and the fragment ion mass tolerance to 0.02 Da. Peptide-spectrum match false discovery rate (FDR) and protein FDR were set to ≤ 0.01. Differentially expressed proteins (DEPs) between control and OSAHS s-EVs were identified using the “Limma” R package (Bioconductor, Walter and Eliza Hall Institute of Medical Research, Melbourne, Australia) with a threshold of  $|\log_2\text{FC}| > 0.5$  and a *P*-value < 0.05.

### 2.12. Gene Ontology (GO) and Kyoto Encyclopedia of Genes and Genomes (KEGG) enrichment analysis

The DEPs were subjected to GO and KEGG pathway enrichment analyses using the “clusterProfiler”, “org.Mm.eg.db”, “enrichplot”, and “ggplot2” packages in R. Circular plots were generated to

visualize the enrichment results of genes corresponding to DEPs in GO categories, including biological processes, cellular components, molecular functions, as well as KEGG enrichment analysis results.

### 2.13. Metabolomics analysis

Serum samples were thawed at room temperature, and 300 µL of each sample was transferred to a 1.5 mL polypropylene tube. The samples were mixed with 900 µL of 80% methanol and 0.1% formic acid, vortexed for 2 min, and centrifuged at 12,000 g for 10 min. The supernatant was transferred to an autosampler vial.

Serum metabolomics analysis was performed using an LC20 ultra-high-performance liquid chromatography (UHPLC) system (Shimadzu Corporation, Kyoto, Japan) coupled with a Triple TOF-6600 mass spectrometer (AB Sciex, Framingham, MA, USA). Separation was achieved using an ACQUITY UHPLC T3 column (100 mm × 2.1 mm, 1.8 µm; Waters Corporation). The mobile phase included 0.1% formic acid in water (Phase A) and 0.1 % formic acid in acetonitrile (Phase B). A 2 µL sample was injected in both positive and negative electrospray ionization (ESI) modes.

The elution gradient was programmed as follows: 5% B (0–2 min), 5%–25% B (2–4 min), 25%–50% B (4–8 min), 50%–80% B (8–10 min), 80%–100% B (14–15 min), 100%–5% B (15–15.1 min), and 5% B (15.1–16 min). The flow rate was 0.35 mL/min. Key mass spectrometry settings included spray voltages of 3,800 V (positive mode) and –3,000 V (negative mode), a capillary temperature of 320 °C, and a mass range of 100–1,000 *m/z*.

Orthogonal partial least squares discriminant analysis (OPLS-DA) and permutation tests (100 permutations) were applied to prevent overfitting. Metabolites with variable importance in projection (VIP) scores > 1 and *P*-values < 0.05 in the OPLS-DA model were identified as differentially expressed metabolites (DEMs). Metabolites with fold changes ≥ 2 or ≤ 0.5, along with a *P*-value < 0.05 in a Student's *t*-test, were further validated through univariate analysis. Pathway analysis was performed using MetaboAnalyst (version 5.0, McGill University, Montreal, Canada).

### 2.14. Integrated analysis of proteomics and metabolomics

Metabolites present in less than 20% of samples were excluded from analysis. Differences in protein abundance between Ctrl-s-EVs and OSAHS-s-EVs were calculated using a linear model in the R package, with multiple testing corrections applied using the Benjamin and Hochberg FDR method (*P* < 0.05). Volcano plots were generated using ggplot2 in R. A protein-metabolite interaction network was constructed to display the functional relationships between DEPs and DEMs, with correlations calculated via Pearson's method to reveal common pathways.

### 2.15. Cell interventions and grouping

To investigate the effects of EVs from different treatment groups on cells, s-EVs were isolated and extracted from experimental groups of mice: NO group, CIH group, CIH + sh-NC group, and CIH + sh-FASN group. The cell groups were labeled as follows: NO + s-EVs group: s-EVs isolated from NO-fed mice were co-cultured with cells; CIH + s-EVs group: s-EVs isolated from mice under intermittent hypoxia conditions were co-cultured with cells; CIH + s-EVs-sh-NC: s-EVs isolated from mice fed with intermittent hypoxia and infected with sh-NC lentivirus were co-cultured with cells; CIH + s-EVs-sh-FASN: s-EVs isolated from mice fed with intermittent hypoxia and infected with sh-FASN lentivirus were co-cultured with cells. Cells were cultured under NO conditions, and each experiment was independently repeated three times.

### 2.16. Endothelial cell uptake of EVs

EVs were labeled with PKH67 (MINI67-1 KT, Sigma-Aldrich, St. Louis, MO, USA) in PBS for 5 min at room temperature, followed by incubation with 1% BSA to stop the labeling process. Labeled EVs (10 mg) were added to mouse aortic endothelial cells (MAECs) (HTX2258, Huatuo Bio, Shanghai, China) and cultured for 6, 12, and 24 h. After washing and fixation, cells were stained with DAPI and visualized under a confocal microscope (Olympus Corporation, Tokyo, Japan). The stained cells were analyzed using ImageJ software.

### 2.17. Detection of total reactive oxygen species (ROS) and mitochondrial ROS

The study utilized the fluorescent dye 2',7'-dichlorodihydrofluorescein diacetate (DCFDA) (HY-D0940, Abcam) to detect ROS in cells. A 10 mM stock solution of DCFDA was prepared in methanol and diluted in the culture medium to a working concentration of 100  $\mu$ M. MAECs ( $2 \times 10^4$ ) were seeded onto glass coverslips in six-well plates and incubated overnight. In the following day, cells were treated with 200  $\mu$ M H<sub>2</sub>O<sub>2</sub> for 24 h. After treatment, the coverslips were washed with ice-cold Hank's balanced salt solution (HBSS) (H8264, Sigma Aldrich) and incubated with 100  $\mu$ M DCFDA at 37 °C for 30 min. After washing with 1  $\times$  PBS, the coverslips were mounted on slides, and images were captured using a multiphoton confocal microscope (A1R, Nikon Corporation, Tokyo, Japan) with a  $\times 100$  objective. Image analysis was performed using Nikon Imaging Software.

To assess mitochondrial superoxide levels, mito-SOX red dye (M36008, Thermo Fisher) was used. MAECs ( $2 \times 10^4$ ) were seeded onto glass coverslips in six-well plates and incubated overnight. The next day, cells were treated with 200  $\mu$ M H<sub>2</sub>O<sub>2</sub> for 24 h. Coverslips were then washed with ice-cold 1  $\times$  PBS and incubated with a working solution of 2  $\mu$ M mito-SOX at 37 °C for 30 min. After washing with 1  $\times$  PBS, the coverslips were mounted on slides. Images were captured using a multiphoton confocal microscope with a  $\times 100$  objective, and analysis was conducted with Nikon Imaging Software.

### 2.18. 5,5',6,6'-tetrachloro-1,1',3,3'-tetraethylbenzimidazolylcarbocyanine iodide (JC-1) staining

For JC-1 staining, MAECs ( $2 \times 10^4$ ) were seeded onto 35 mm culture plates and incubated overnight. They were co-cultured with s-EVs from different groups the following day for 24 h. Subsequently, the cells were washed three times with 1  $\times$  PBS and incubated with JC-1 dye (T3168, Thermo Fisher) at 37 °C for 20 min. After washing the cells with 1  $\times$  PBS, they were mounted on slides and observed under a fluorescence microscope [22].

### 2.19. Western blot

Total proteins were extracted from s-EVs, MAECs, and mouse arterial tissues. Cells were digested with trypsin (T4799-5G, Sigma-Aldrich) and lysed using an enhanced radioimmunoprecipitation assay (RIPA) buffer containing protease inhibitors (ARO108, Doctor's Lab, Wuhan, China). Protein concentrations were measured using a BCA protein quantification kit (AR1189, Doctor's Lab). Proteins were separated by sodium dodecyl sulfate–polyacrylamide gel electrophoresis (SDS-PAGE), transferred onto polyvinylidene difluoride (PVDF) membranes, and blocked with 5% BSA (9048-46-8, Solarbio) at room temperature for 1 h.

The membranes were incubated overnight at 4 °C with primary antibodies (Table S3), washed three times with PBST, and incubated

with secondary antibodies (Anti-Mouse-HRP, Cat # 7076, or Anti-Rabbit-HRP, Cat # 7074, Cell Signaling Technology, Danvers, MA, USA) at 1:5000 dilution for 1 h at room temperature. After additional washes with PBST, the membranes were developed using enhanced chemiluminescence (ECL) substrate (Omt-01, Beijing Omjia Medical Technology Co., Ltd., Beijing, China). The blots were exposed for 5–10 min in a dark box, then developed and fixed. Grayscale quantitative analysis of the bands was performed using ImageJ software, with  $\beta$ -tubulin or GAPDH as internal controls [23].

### 2.20. Endothelial cell apoptosis assay

s-EVs from various treatment groups were co-cultured with MAECs for 24 h. Apoptosis levels were assessed using Annexin V-PI (CA1020, ACMEC, Shanghai, China) and TUNEL (11684795910, Roche Diagnostics, Indianapolis, IN, USA) according to the manufacturer's instructions.

#### 2.20.1. TUNEL staining

Cells were treated with proteinase K and 3 % hydrogen peroxide, incubated with the TUNEL reaction mixture at 37 °C in a humid chamber, and washed with TBST. The cells were then stained with DAPI solution (D1306, Thermo Fisher) for nuclear visualization and observed under a fluorescence microscope [24].

#### 2.20.2. Flow cytometry

Cells were collected, washed with pre-chilled PBS, and stained with Annexin V-fluorescein isothiocyanate (FITC) and propidium iodide (PI) from the apoptosis kit at 4 °C for 10 min. The cell death rate (105 cells per sample) was determined using a CytoFlex flow cytometer (Beckman Coulter). Cell phenotypes were categorized based on their quadrant positions: Annexin V<sup>+</sup>PI<sup>+</sup> (late apoptosis), Annexin V<sup>+</sup>PI<sup>-</sup> (early apoptosis), Annexin V<sup>-</sup>PI<sup>+</sup> (necrosis), and Annexin V<sup>-</sup>PI<sup>-</sup> (live cells) [25]. Data analysis was performed using FlowJo software (Version 7.0), with forward scatter (FSC) and side scatter (SSC) set as logarithmic axes and quadrants used to distinguish live and apoptotic cells. The apoptosis rate was calculated as the sum of Annexin V-positive cells (early and late apoptosis).

### 2.21. Enzyme-linked immunosorbent assay (ELISA)

Serum samples from patients and mice were collected by allowing whole blood to clot for 20–30 min at room temperature, followed by centrifugation at 2,000 g for 10 min. The serum was stored at –80 °C until further use.

The following ELISA kits were utilized: IL-1 $\beta$  ELISA Human Kit (ab214025, Abcam), IL-1 $\beta$  ELISA Mouse Kit (ab197742, Abcam), CRP ELISA Human Kit (ab278042, Abcam), ET-1 ELISA Human and Mouse Kit (ab133030, Abcam), TNF- $\alpha$  ELISA Mouse Kit (ab183218, Abcam), MCP-1 Mouse Kit (ab208979, Abcam), and CRP ELISA Mouse Kit (ab222511, Abcam).

Antigens were diluted to the appropriate concentration, and wells were blocked with 5% bovine serum (F8318, MSK, Wuhan, China) at 37 °C for 40 min. Diluted samples were added to the wells along with enzyme-labeled antibodies and substrate solutions. After adding 50  $\mu$ L of stop solution, results were recorded within 20 min. Optical density was measured at 450 nm using a Bio-Rad microplate reader (Bio-Rad Laboratories, Hercules, CA, USA), and data was analyzed by constructing a standard curve [26].

### 2.22. Scratch experiment

MAECs were seeded and cultivated in a 24-well plate. Once the cells reached confluence, they were scratched with a 200  $\mu$ L pipette tip, washed with PBS, and then incubated for 48 h in Roswell Park

Memorial Institute 1640 (RPMI 1640) medium without FBS. Photos were taken at the beginning and end of the experiment at 5× magnification using an inverted microscope. The scratch area was analyzed using ImageJ software to calculate the wound healing rate [27].

### 2.23. Serum phosphate (Pi) and NO assessment

Pi levels in human or mouse serum were measured using a phosphate colorimetric test kit (molybdenum method) (E-BC-K245-S, Wuhan Elisa Biotech Co., Wuhan, China). Inorganic phosphates reacted with molybdic acid to form phosphomolybdate, which was reduced to molybdenum blue. The absorbance at 660 nm was proportional to the phosphate concentration.

Nitric oxide (NO) levels in serum were assessed using an NO colorimetric test kit (E-BC-K035-M, Wuhan Elisa Biotech Co., Ltd.). NO oxidized to form NO<sub>2</sub>, which generated a light red azo compound. The color intensity was used to calculate the NO concentration [28].

### 2.24. Adenosine triphosphate (ATP) content detection

MAECs (1 × 10<sup>5</sup>/well) were co-incubated with s-EVs from different groups in a 6-well plate. Total cellular ATP was extracted and measured using an ATP assay kit (BC0300, Solarbio) according to the manufacturer's protocol. ATP levels were quantified using a ultraviolet-visible (UV) spectrophotometer (DU720, Beckman Coulter) [29].

### 2.25. Metabolic analysis

The Seahorse XFe96 extracellular flux analyzer (Agilent Technologies, Santa Clara, CA, USA) was used for metabolic analysis. Cells (12,000/well) were cultured in Seahorse plates, and reagents for the glycolysis stress test included 10 mM glucose (50-99-7, Sigma-Aldrich), 2 μM oligomycin (1404-19-9, Sigma-Aldrich), and 50 mM 2-deoxy-D-glucose (154-17-6, Sigma-Aldrich). For the mitochondrial stress test, cells were treated with glucose, followed by 1 mM oligomycin, 1 mM carbonyl cyanide 4-(trifluoromethoxy) phenylhydrazone (FCCP), and 0.5 mM antimycin A (a mitochondrial complex III inhibitor used in mitochondrial stress tests)/rotenone (Sigma-Aldrich). The XF Glycolysis and Cell Mito Stress Test Kits were purchased from Agilent Technologies [30,31].

### 2.26. Cell co-culture

THP-1 monocytes (TIB-202, ATCC) were cultured in a 6-well plate treated with 100 nM phorbol 12-myristate 13-acetate (PMA) (Sigma-Aldrich) for 24 h, inducing their differentiation into adherent macrophages, hereafter referred to as THP-P [32]. After co-culturing different treatment groups' s-EVs with THP-P cells for 24 h, the cells were seeded onto the upper chamber of a Transwell system. Meanwhile, MAECs were seeded in the lower chamber of the Transwell system and co-cultured with THP-P for 24 h to observe cell adhesion and the expression of inflammatory factors in endothelial cells.

### 2.27. Static adhesion assay

THP-P cells were pre-stained with 5 μM Calcein-AM (C1429, Invitrogen, Carlsbad, CA, USA) for 30 min, washed in PBS, and then added to a monolayer of MAECs at a 10<sup>6</sup> cells/mL density. After 30 min, non-adherent monocytes were gently washed off with a complete culture medium. The fluorescence intensity (FI) was measured using the Infinite F200 fluorescence ELISA reader

(TECAN, Männedorf, Switzerland) at excitation and emission wavelengths of 485 and 530 nm [33].

### 2.28. 3-(4,5-Dimethylthiazol-2-yl)-2,5-diphenyltetrazolium bromide (MTT) cell viability assay

Cells were seeded in a 96-well plate at a density of 1 × 10<sup>4</sup> cells per well and incubated for 24 h. Subsequently, cells from different treatment groups were cultured with 0.5 mg/mL MTT (298-93-1, Sigma-Aldrich) in the presence or absence of 10 mM 3-MA (5142-23-4, Sigma Aldrich) or 1 μM wortmannin (19545-26-7, MedChemExpress, Monmouth Junction, NJ, USA) for 4 h in the culture medium. Cell viability was determined by measuring the absorbance at 570 nm [34].

### 2.29. Statistical analysis

All data were analyzed using GraphPad Prism 8.0, and quantitative data were presented as mean ± standard deviation (SD). Statistical comparisons between two groups were performed using unpaired *t*-tests, while comparisons among multiple groups were carried out using one-way analysis of variance (ANOVA). Homogeneity of variance was tested using the Levene method, and pairwise comparisons were conducted using Dunnett's *t* and least significant difference *t*-tests (LSD)-*t* tests for homogeneous variances. In cases of inhomogeneous variance, Dunnett's T3 test was applied. A significance level of *P* < 0.05 indicated statistically significant differences between groups [35].

## 3. Results

### 3.1. Correlation study of serum CRP levels and disease severity in OSAHS patients

To investigate the correlation between serum CRP levels and disease severity in OSAHS patients, we selected clinical OSAHS patients for our study. Table S1 presents the clinical and laboratory characteristics of OSAHS patients and the control group. Compared to the healthy control group, OSAHS patients showed elevated CRP levels. There were no significant differences in age, BMI, SBP, DBP, FPG, serum TC, TG, LDL-C, and HDL-C between the two groups. Sleep characteristics for both groups are detailed in Table S4. OSAHS patients exhibited higher levels of AHI, percentage of total sleep time with SaO<sub>2</sub> <90% (TST), oxygen desaturation index (ODI), and epworth sleepiness scale (ESS) scores compared to the healthy control group, while average and minimum SPO<sub>2</sub> levels were lower.

### 3.2. OSAHS patient-derived s-EVs induce lung endothelial dysfunction

Intermittent hypoxia, a key feature of OSAHS, induces changes in plasma s-EVs [13]. To examine the effects of s-EVs on lung endothelial injury, we isolated s-EVs from OSAHS and non-OSAHS patients using ultracentrifugation. TEM confirmed that s-EVs from both groups had similar morphology and size, with diameters less than 100 nm (Figs. S1A and B). Western blot analysis showed significant upregulation of CD9, HSP70, and CD63 in s-EVs, while serum albumin was absent, confirming successful s-EV isolation (Fig. S1C). Quantification of s-EVs revealed higher concentrations and protein content in OSAHS patients compared to controls (Figs. S1D and E). Inflammatory markers such as CRP were also enriched in OSAHS-derived s-EVs (Fig. S1F).

PKH26-labeled s-EVs from OSAHS and control patients were injected into mice cultured under NO and CIH conditions. s-EVs were distributed in lung tissues, and hematoxylin and eosin (H&E)

staining revealed significant inflammatory cell infiltration and pulmonary edema, particularly in the CIH + OSAHS s-EVs group (Figs. 1A and B). Apoptosis rates and inflammatory cytokines (tumor necrosis factor- $\alpha$  (TNF- $\alpha$ ), interleukin-6 (IL-6), monocyte chemoattractant protein-1 (MCP-1)) were significantly higher in NO + OSAHS s-EVs and CIH groups, with the highest levels in the CIH + OSAHS s-EVs group (Figs. 1C and D). CIH + OSAHS s-EVs also led to increased ROS levels, myeloperoxidase (MPO) activity, and malondialdehyde (MDA) content in lung tissues, along with reduced superoxide dismutase (SOD) activity (Figs. 1E–H). Immunohistochemistry revealed reduced CD31/ $\alpha$ -SMA positive cells in the CIH + OSAHS s-EVs group, indicating lung endothelial dysfunction (Fig. 1I).

These results indicate that s-EVs derived from OSAHS patients can induce lung endothelial dysfunction.

### 3.3. Molecular mechanisms of s-EVs inducing endothelial dysfunction in OSAHS, differential expression protein characteristics, and metabolomic features

To explore the molecular mechanisms, we performed iTRAQ-based proteomics on s-EVs from OSAHS and non-OSAHS patients. Principal component analysis (PCA) revealed significant differences in protein spectra between groups (Fig. S2A). SDS-PAGE analysis showed even protein distribution (Fig. S2B), and clustering analysis confirmed distinct protein expression patterns in s-EVs from

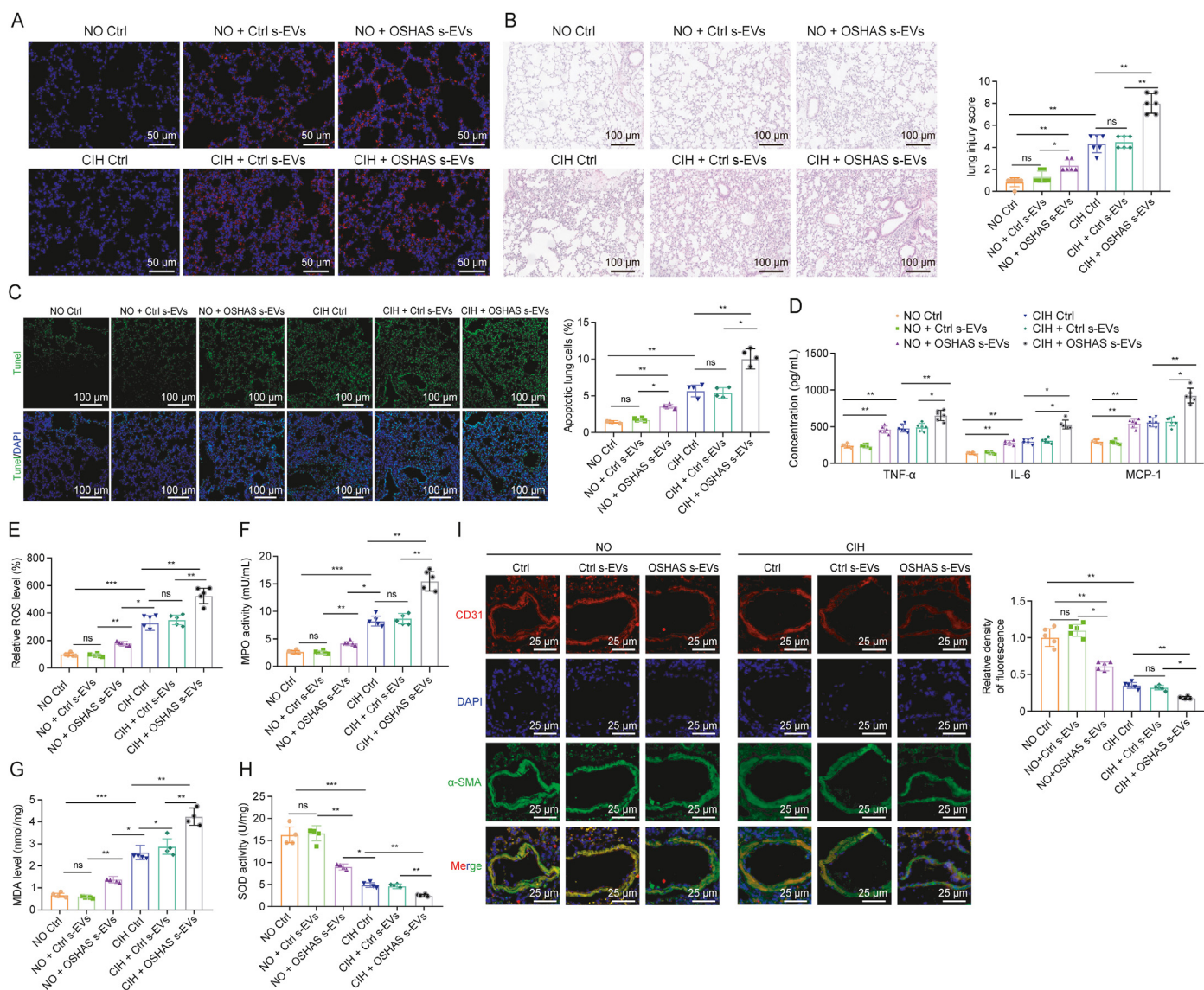


**Fig. 1.** The impact of serum-derived extracellular vesicles (s-EVs) on lung endothelial function in patients with obstructive sleep apnea hypopnea syndrome (OSAHS). (A) Distribution of s-EVs labeled with PKH26 in lung tissue. (B) Observation of lung tissue morphology and lung injury scoring statistics with hematoxylin and eosin (H&E) staining. (C) Determination of terminal deoxynucleotidyl transferase-mediated dUTP nick end labeling (TUNEL) positivity rate in lung tissue using TUNEL staining. (D) Measurement of tumor necrosis factor- $\alpha$  (TNF- $\alpha$ ), interleukin-6 (IL-6), and monocyte chemoattractant protein-1 (MCP-1) levels using enzyme-linked immunosorbent assay (ELISA) assay. (E–H) Assessment of reactive oxygen species (ROS) levels (E), myeloperoxidase (MPO) activity (F), malondialdehyde (MDA) levels (G), and superoxide dismutase (SOD) activity (H) in lung tissue. (I) Estimation of endothelial integrity in vascular cross-section using cluster of differentiation 31 (CD31) fluorescence intensity. Each group consisted of 6 mice, and values are presented as mean  $\pm$  standard deviation (SD), where \* $P$  < 0.05 denotes significance, \*\* $P$  < 0.01 denotes high significance, \*\*\* $P$  < 0.001, and ns indicates non-significance. NO: normoxia; Ctrl: control; DAPI: 4',6-diamidino-2-phenylindole;  $\alpha$ -SMA:  $\alpha$ -smooth muscle actin.

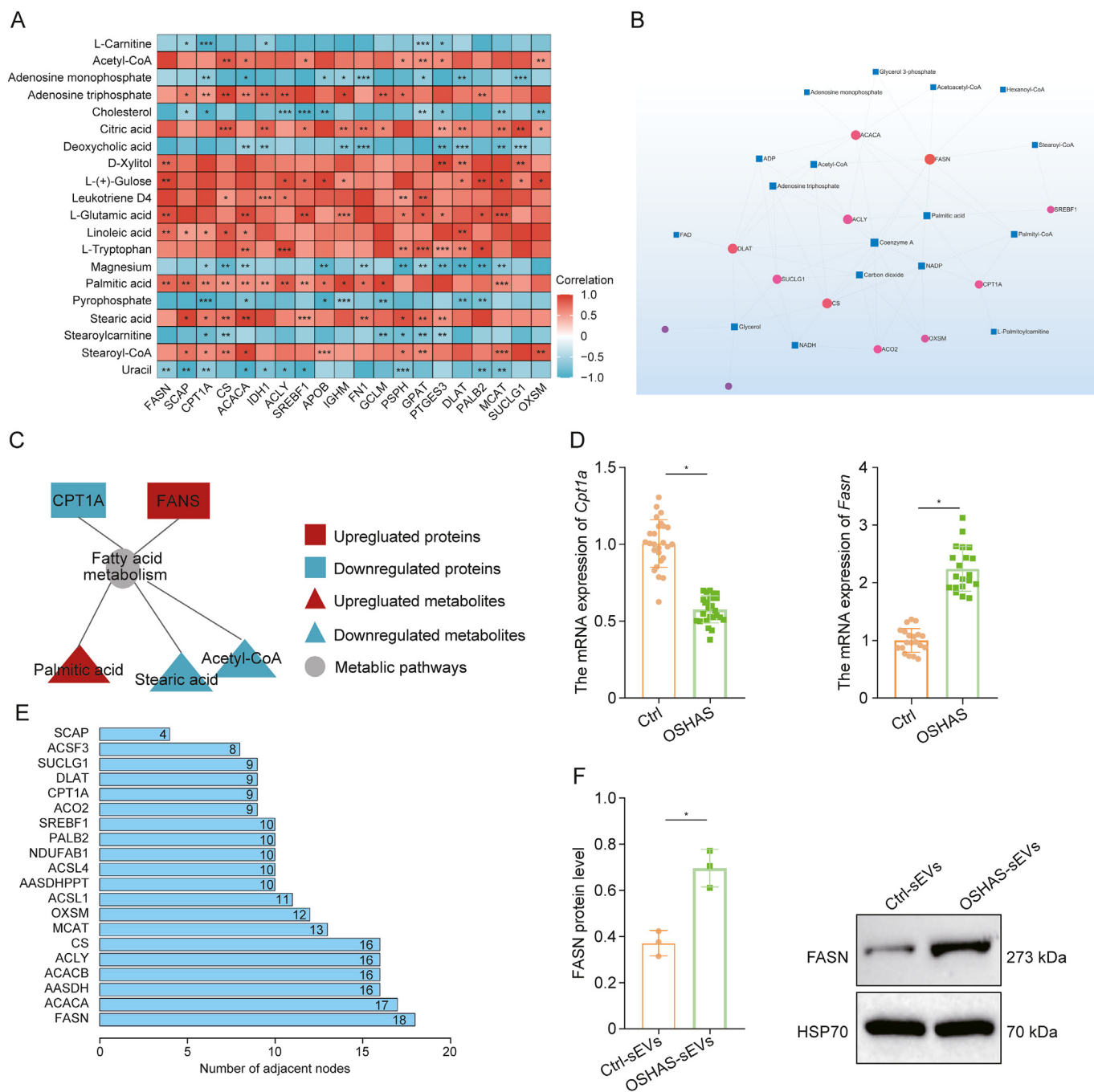


**Fig. 2.** Joint analysis of differentially expressed proteins (DEPs) and metabolites. (A) Correlation heatmap of the results between DEPs and differentially expressed metabolites (DEMs), where orange to red indicates a positive correlation and blue indicates negative correlation. (B) Significant association network between DEPs and DEMs, where circles represent DEPs, squares represent DEMs, and darker colors indicate higher correlation. (C) Joint Gene Ontology (GO) and Kyoto Encyclopedia of Genes and Genomes (KEGG) analysis of DEPs-DEMs lipid metabolism network, where red indicates upregulated proteins or metabolites, blue indicates downregulated proteins or metabolites, and gray indicates metabolic pathways. (D) Quantitative polymerase chain reaction (qPCR) shows changes in arniten palmitoyltransferase 1A (*Cpt1a*) and fatty acid synthase (*Fasn*) expression in obstructive sleep apnea hypopnea syndrome (OSAHS) mouse group ( $n = 20$ ). (E) Protein correlation analysis involved in lipid metabolism. (F) Western blot detection of FASN protein expression in Ctrl s-EVs and OSHAS s-EVs ( $n = 3$ ). \* $P < 0.05$  indicates significance, \*\* $P < 0.001$  indicates high significance, \*\*\* $P < 0.001$  indicates very high significance, and ns indicates non-significance at  $P > 0.05$  between the two groups. Ctrl: control; s-EVs: serum-derived extracellular vesicles.

OSAHS patients (Figs. S2C and D). In s-EVs from OSAHS patients and control groups, we identified 2,756 proteins, with 206 DEPs, including 144 upregulated and 102 downregulated proteins (Fig. S2E). GO and KEGG analyses revealed that these proteins are enriched in the top 20 functional categories (Figs. S2F–I), primarily involving coagulation, carbohydrate metabolism, cell adhesion, protein binding, peptidase activity, cholesterol accumulation,

inflammatory factors, and complement activation. The DEPs also showed enrichment in mitochondrial membranes, extracellular vesicle release, carbohydrate metabolism, apoptosis regulation, and calcium ion binding (Figs. S2B–D). Of particular note within these categories is the close association of inflammation with glucose metabolism, amino acid metabolism, fatty acid metabolism, energy metabolism, and the PPAR signaling pathway (Fig. S2F). These

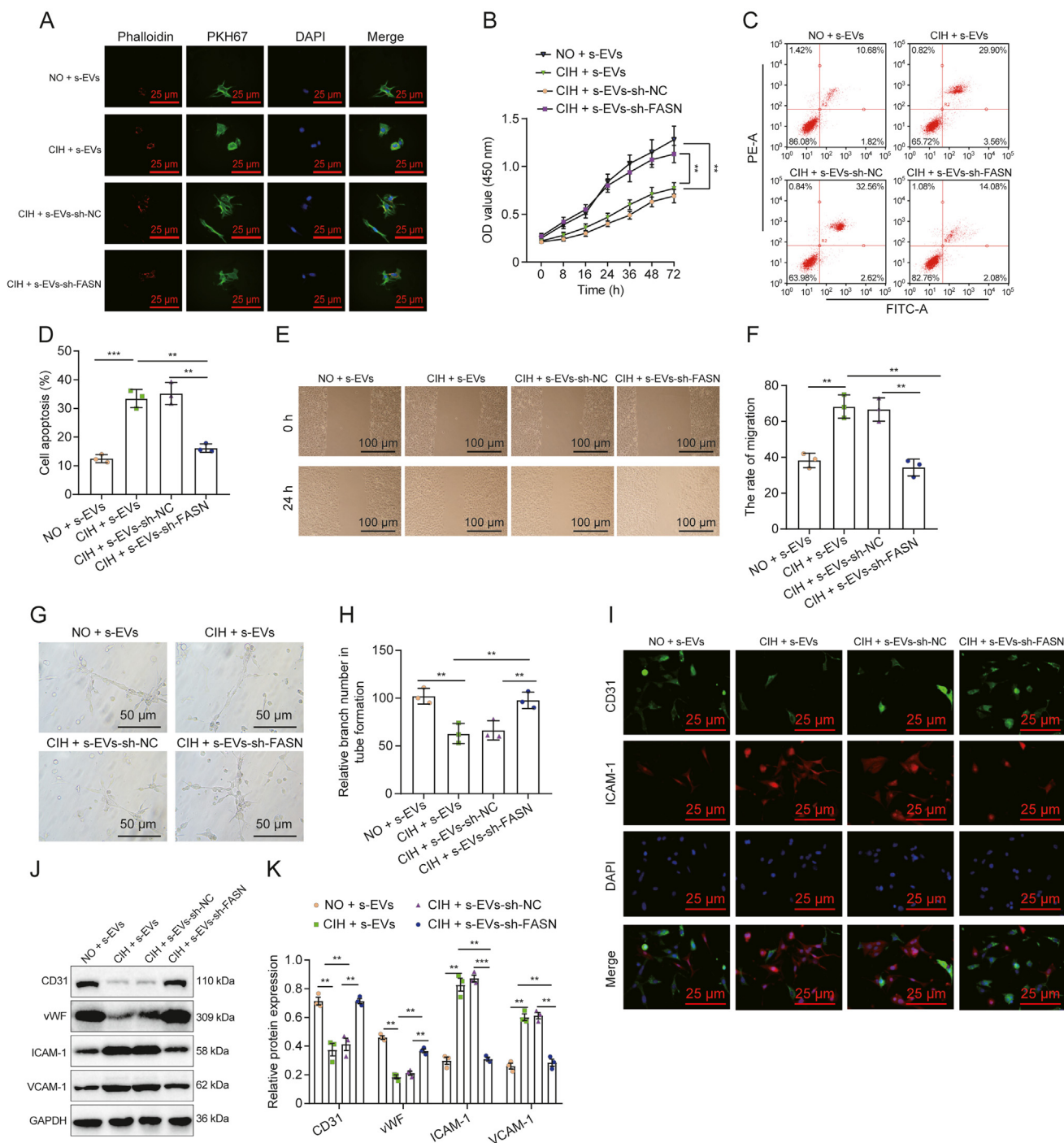


**Fig. 3.** The influence of serum-derived extracellular vesicles (s-EVs) from chronic intermittent hypoxia (CIH) mice on endothelial function. (A) Confocal microscopy images of uptake of PKH67-labeled s-EVs across mouse aortic endothelial cells (MAECs). (B) Methylthiazolylidiphenyl-tetrazolium bromide (MTT) assay detecting endothelial cell viability in different treatment groups; (C, D) Flow cytometry assessment of cell apoptosis in different treatment groups. (E, F) Scratch assay measuring cell migration in different treatment groups (E) and the statistic plot (F). (G, H) Matrigel tube formation assay determining the tube-forming ability of MAECs in different treatment groups (G) and the statistic plot (H). (I) Immunofluorescence images of cluster of differentiation 31 (CD31) (green fluorescence) and intercellular adhesion molecule-1 (ICAM-1) (red fluorescence) staining in MAECs. (J, K) Western blot experiments measuring levels of endothelial dysfunction markers CD31, von Willebrand factor (vWF), ICAM-1, and vascular cell adhesion molecule-1 (VCAM-1) in different treatment groups (J) and the statistic plot (K). \*\**P* < 0.001 denotes high significance, \*\*\**P* < 0.001 denotes very high significance, with cell experiments repeated three times. OSAS: obstructive sleep apnea hypopnea syndrome; NO: normoxia; sh-NC: control shRNA; sh-FASN: FASN-targeting shRNA; CIH: chronic intermittent hypoxia; DAPI: 4',6-diamidino-2-phenylindole.

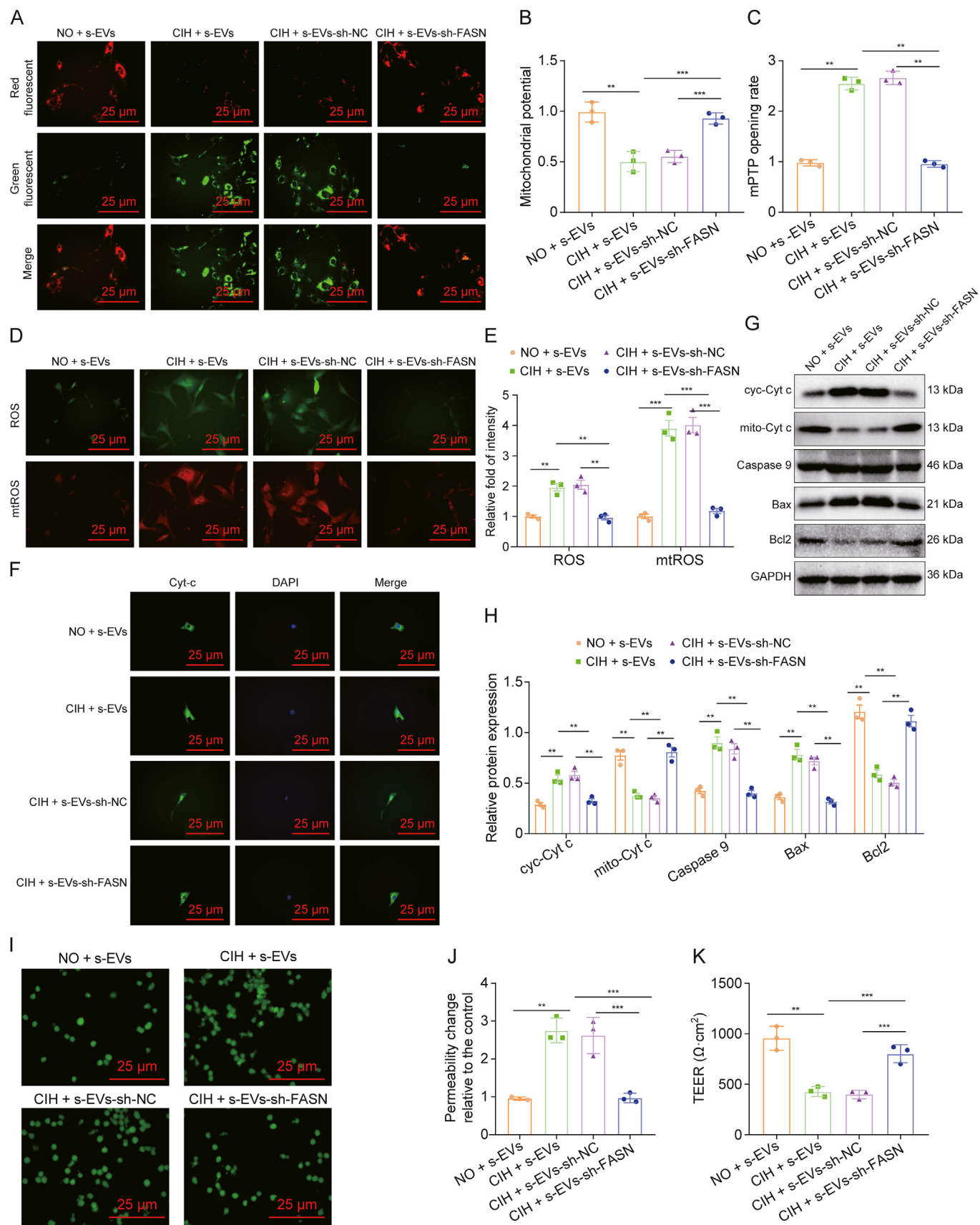


**Fig. 4.** Fatty acid synthase (FASN) activation mediates mitochondrial dysfunction-induced endothelial cell apoptosis. (A) Evaluation of endothelial cell mitochondrial membrane potential (MMP) using 5,5',6,6'-tetrachloro-1,1',3,3'-tetraethylbenzimidazolylcarbocyanine iodide (JC-1) showing aggregates (red) and monomers (green). (B) The statistic plot of monomers (green). (C) Mitochondrial permeability transition pore (mPTP) opening rate in different treatment groups. (D) Fluorescence microscopy displaying total reactive oxygen

pathways enhance metabolic effects under intermittent hypoxic conditions, promoting the progression of related diseases.

To investigate the metabolic basis of endothelial dysfunction induced by s-EVs in OSAHS patients, we used ultra-performance liquid chromatography-tandem mass spectrometry (UPLC-MS/MS) and statistical methods to analyze metabolic differences between OSAHS and non-OSAHS groups. PCA and PLS-DA models showed significant metabolic distinctions, with OPLS-DA improving differentiation by reducing noise (Fig. S3A). A total of 401 DEMs were identified, with 110 increased and 102 decreased in OSAHS (Figs. S3B and C). KEGG enrichment highlighted pathways related to fatty acid metabolism, mitochondrial beta-oxidation, and carbohydrate metabolism (Figs. S3D–F), suggesting altered energy metabolism in OSAHS patients. To better understand the impact of OSAHS patient s-EVs on endothelial function, we integrated the obtained proteomics and metabolomics data. Using Pearson correlation analysis for the top 20 DEPs and DEMs, we assessed their correlation and depicted a correlation heatmap (Fig. 2A). The network diagram of DEPs and DEMs highlighted FASN, citrate synthase (CS), ATP citrate lyase (ACLY), and dihydrolipoamide acetyltransferase (DLAT) as key nodes in metabolism (Fig. 2B). Combined GO and KEGG analysis indicated the important roles of FASN and carnitine palmitoyltransferase 1A (CPT1A) in regulating fatty acid metabolism (Fig. 2C). qPCR validation of the mRNA expression of network central proteins showed a significant increase in *Fasn* expression and a decrease in *Cpt1a* expression, consistent with the proteomic analysis results (Fig. 2D). Moreover, network node analysis of enriched lipid metabolism DEPs revealed FASN as the core protein (Fig. 2E). Additionally, we detected the protein expression of FASN in Ctrl s-EVs and OSHA s-EVs, showing a significant increase in FASN protein expression in OSHA s-EVs compared to Ctrl s-EVs (Fig. 2F).

The joint analysis of proteomics and metabolomics in s-EVs of OSHA patients demonstrated that FASN is a core protein involved in lipid metabolism.

### 3.4. FASN inhibits the impact of CIH-induced s-EVs on endothelial cell function

Our proteomics and metabolomics study revealed that FASN is highly expressed in s-EVs of OSHA patients, playing a key role in regulating lipid metabolism. Previous research has shown elevated FASN expression in cardiovascular diseases, including coronary atherosclerosis [19]. Moreover, FASN expression is linked to lipid metabolism and NOS activity in endothelial cells [20], and FASN inhibition can improve endothelial function, reducing inflammation and oxidative stress [21].

To explore the effect of FASN in s-EVs of OSHA patients on endothelial function, we established a mouse model of intermittent hypoxia, manipulating *Fasn* expression (Fig. S4A). We isolated s-EVs from CIH-treated mice (Figs. S4B and C) and found that FASN protein expression increased in s-EVs from CIH-treated mice but decreased after FASN silencing (Fig. S4D). Confocal microscopy revealed similar uptake of PKH67-labeled s-EVs across MAECs after 24 h (Fig. 3A). Post co-incubation with s-EVs, *Fasn* expression was significantly higher in MAECs treated with CIH + s-EV compared to NO + s-EV, but decreased in the CIH + s-EV-sh-FASN group compared to the CIH + s-EV + sh-NC group (Fig. S4E).

Cell viability assays indicated reduced viability in the CIH + s-EV group, while FASN silencing in CIH + s-EV-sh-FASN rescued cell viability (Fig. 3B). Flow cytometry showed increased apoptosis in the CIH + s-EV group, with reduced apoptosis after FASN silencing (Figs. 3C and D). Scratch assays showed impaired cell migration in the CIH + s-EV group, which improved after FASN silencing (Figs. 3E and F). Tube formation assays revealed inhibited angiogenesis in the CIH + s-EV group, with restoration in the CIH + s-EV-sh-FASN group (Figs. 3G and H). Immunofluorescence staining showed decreased CD31-positive and increased ICAM-1-positive cells in the CIH + s-EV group, indicating endothelial injury. Silencing FASN partially reversed these changes (Fig. 3I). Western blot analysis demonstrated upregulation of endothelial dysfunction markers ICAM-1 and vascular cell adhesion molecule-1 (VCAM-1) and downregulation of CD31 and von willebrand factor (vWF) in the CIH + s-EV group compared to the NO + s-EV group, indicating impaired endothelial function, while the CIH + s-EV-sh-FASN group showed reduced expression of ICAM-1 and VCAM-1 and increased expression of CD31 and vWF compared to the CIH + s-EV + sh-NC group, suggesting partial reversal of endothelial dysfunction (Figs. 3J and K).

In conclusion, our results indicate that FASN in CIH-derived s-EVs inhibits endothelial cell proliferation and migration, leading to endothelial injury.

### 3.5. Mitochondrial dysfunction mediated by FASN associated with endothelial cell apoptosis and increased permeability under CIH conditions

Intermittent hypoxia adversely affects mitochondrial function, disrupting normal cellular metabolism and energy supply [36,37]. Under CIH conditions, FASN activation impairs endothelial proliferation and migration, leading to apoptosis and dysfunction. We assessed mitochondrial function to further investigate this relationship. Compared to the NO + s-EV group, CIH + s-EV reduced mitochondrial membrane potential (MMP), while FASN silencing restored MMP (Figs. 4A and B). The decline in MMP is linked to mitochondrial permeability transition pore (mPTP) opening. The CIH + s-EV group induced mPTP openings, while FASN silencing inhibited this effect (Fig. 4C). The opening of mPTP and a decrease in MMP can trigger the activation of the classical mitochondrial apoptosis pathway. Mitochondrial apoptosis is characterized by the overproduction of ROS and leakage of pro-apoptotic factors from mitochondria into the cytosol [38,39]. The CIH + s-EV group produced more mitochondrial ROS, with reduced levels after FASN silencing (Figs. 4D and E). Immunofluorescence showed increased Cyt-c release into the cytosol in the CIH + s-EV group, with reversal in the FASN-silenced group (Fig. 4F). The Western blot results were consistent with the immunofluorescence experiments (Figs. 4G and H).

Cell permeability assays showed that CIH + s-EV treatment significantly increased endothelial permeability compared to the NO + s-EV group. Moreover, silencing FASN markedly reduced permeability in the CIH + s-EV + sh-FASN group relative to the CIH + s-EV-sh-NC group (Figs. 4I and J). The cell resistance measurement results further confirmed the cell permeability experiment results (Fig. 4K).

In conclusion, the study results suggest that FASN-mediated mitochondrial dysfunction leads to endothelial cell apoptosis and increased cell permeability.

species (ROS) levels and mitochondrial ROS (mtROS) levels, with ROS (green) and mtROS (red). (E) Fluorescence microplate showing ROS and mtROS. (F) Immunofluorescence detecting leakage of mitochondrial Cytochrome c (Cyt c) into the cytoplasm and nucleus. (G, H) Western blot analysis of changes in mitochondrial apoptosis proteins (G) and the statistical plot (H). (I, J) Observation of cell permeability in different treatment groups (I) and the statistic plot (J). (K) Changes in cell resistance in different treatment groups. \*\* $P < 0.01$  denotes high significance, and \*\*\* $P < 0.001$  denotes very high significance, with cell experiments repeated three times. NO: normoxia; CIH: chronic intermittent hypoxia; sh-NC: control shRNA; sh-FASN: FASN-targeting shRNA; s-EVs: serum-derived extracellular vesicles; cyc-Cyt c: cytochrome c in the cytosolic fraction; GAPDH: glyceraldehyde-3-phosphate dehydrogenase.

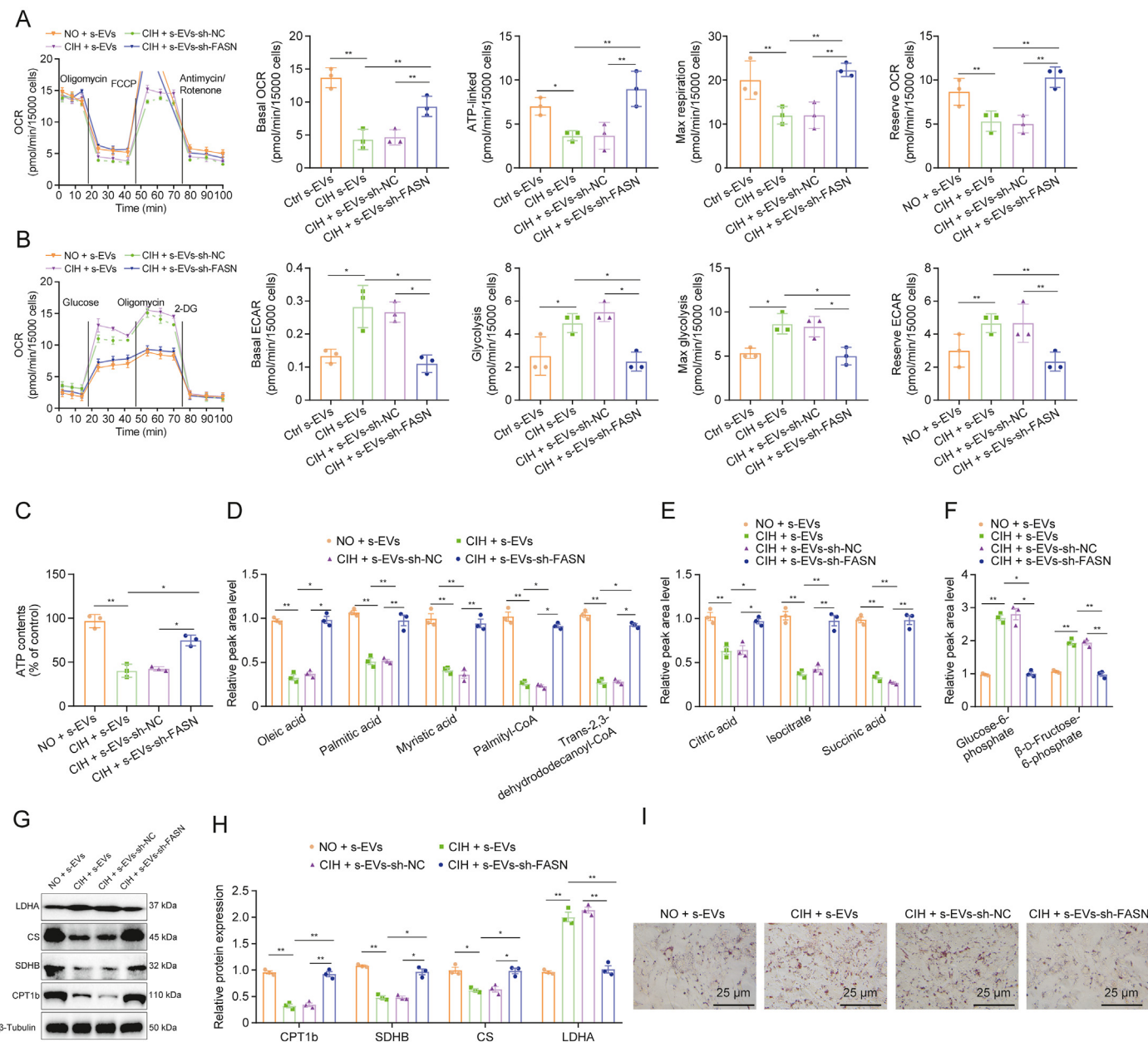


**Fig. 5.** Regulation of energy metabolism by fatty acid synthase (FASN) under chronic intermittent hypoxia (CIH) conditions. (A) Seahorse XFe96 was used to measure oxygen consumption rate (OCR). Respective components of OCR via calculation as follows: Basal OCR = pre oligomycin – post antimycin/rotenone, adenosine triphosphate (ATP)-linked = pre oligomycin – post oligomycin, Max respiration = post carbonyl cyanide 4-(trifluoromethoxy)phenylhydrazone (FCCP) – post antimycin/rotenone, and Reserve OCR = post FCCP – pre FCCP. (B) Seahorse XFe96 was used to measure extracellular acidification rate (ECAR). Respective ECAR components with calculations as follows: Basal ECAR = pre glucose – post 2-deoxyglucose (2-DG), Glycolysis = post glucose – pre glucose, Max glycolysis = post oligomycin – post 2-DG, and Reserve ECAR = post oligomycin – pre oligomycin.  $n = 11–12$  individual replicates per group. (C) Mitochondrial ATP quantification analysis. (D–F) Measurement of metabolite levels related to fatty acid β-oxidation (D), tricarboxylic acid (TCA) (E), and glycolysis (F) in mitochondria. (G, H) Analysis of enzyme levels related to fatty acid β-oxidation, TCA cycle, and glycolysis in mitochondria using Western blot (G), and quantitative data (H). (I) Observation of changes in intracellular lipid droplets in different treatment groups through Oil Red O staining. \* $P < 0.05$  indicates a significant difference between the two groups, \*\* $P < 0.01$  indicates a significant difference, with the cell experiments repeated three times. NO: normoxia; s-EVs: serum-derived extracellular vesicles; sh-NC: control shRNA; sh-FASN: FASN-targeting shRNA; CPT1b: carnitine palmitoyltransferase 1b; SDHB: succinate dehydrogenase complex subunit B; CS: citrate synthase; LDHA: lactate dehydrogenase A.

### 3.6. The role of FASN in regulating endothelial cell energy metabolism and lipid accumulation

While endothelial cells primarily rely on glycolysis for energy, recent research has highlighted the importance of fatty acid oxidation (FAO) in generating acetyl-CoA and NADPH [40]. NADPH produced from endothelial FAO helps maintain redox balance in the tricarboxylic acid cycle (TCA), which regulates endothelial

activation and controls permeability. Additionally, FAO in endothelial cells supports biomass synthesis and the production of deoxyribonucleotide triphosphates (dNTPs), which are essential for DNA synthesis during cell proliferation [41].

Mitochondrial respiration and glycolytic function were evaluated through oxygen consumption rate (OCR) and extracellular acidification rate (ECAR) spectra. Compared to the NO + s-EV group, the CIH + s-EV group exhibited decreased baseline OCR,

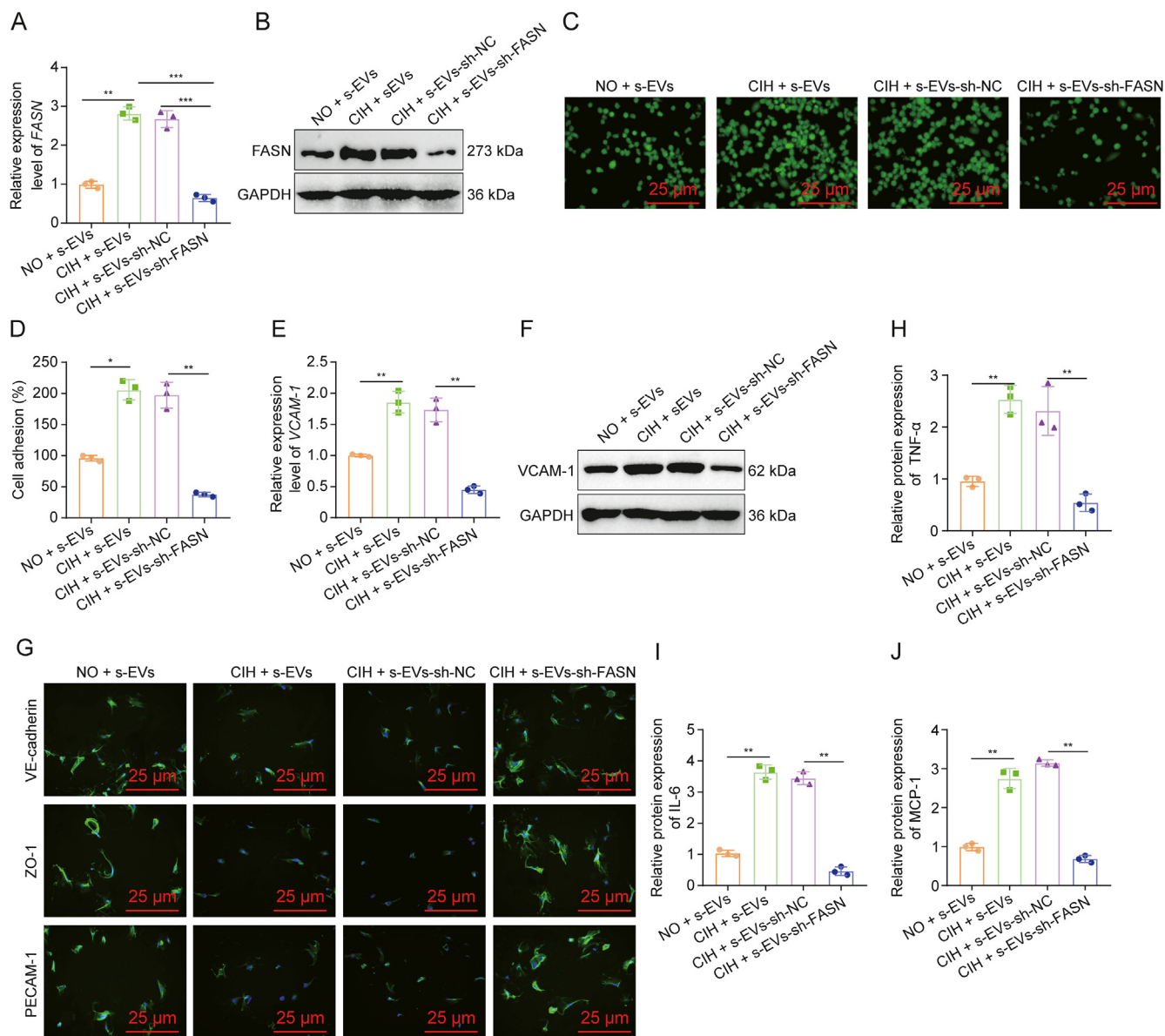


**Fig. 6.** Fatty acid synthase (FASN) modulates cell adhesion behavior to promote inflammatory factor aggregation in endothelial cells. (A) Reverse transcription-quantitative polymerase chain reaction (RT-qPCR) was used to detect the expression level of FASN in THP-P cells. (B) Western blot was applied to determine the protein expression of FASN in THP-P cells. (C, D) Assessment of cell adhesion in different treatment groups (C) and the statistical data (D). (E, F) Measurement of vascular cell adhesion molecule-1 (VCAM-1) expression in cells through RT-qPCR (E) and Western blot (F). (G) Observation of changes in cell adhesion molecules using immunofluorescence. (H–J) Evaluation of the expression of inflammatory factors tumor necrosis factor- $\alpha$  (TNF- $\alpha$ ) (H), interleukin-6 (IL-6) (I), monocyte chemoattractant protein-1 (MCP-1) (J) in endothelial cells via Western blot. \* $P < 0.05$  indicates a significant difference between the two groups, \*\* $P < 0.01$  indicates a significant difference, and \*\*\* $P < 0.001$  indicates a very highly significant difference between the two groups, with the cell experiments repeated three times. NO: normoxia; s-EVs: serum-derived extracellular vesicles; CIH: chronic intermittent hypoxia; sh-NC: control shRNA; sh-FASN: FASN-targeting shRNA; PECAM-1: platelet endothelial cell adhesion molecule-1; ZO-1: zonula occludens-1; GAPDH: glyceraldehyde-3-phosphate dehydrogenase.

maximum, and spare respiratory capacities. The CIH + s-EV-sh-FASN group showed improved baseline OCR, maximum, and spare respiratory capacities compared to the CIH + s-EV + sh-NC group (Fig. 5A). The glycolytic capacity and reserve were elevated in the CIH + s-EV group compared to the NO + s-EV group. The CIH + s-EV-sh-FASN group downregulated glycolysis compared to the CIH + s-EV + sh-NC group (Fig. 5B). ATP generation significantly decreased in the CIH + s-EV group compared to the NO + s-EV group. Silencing FASN in the CIH + s-EV-sh-FASN group rescued ATP production compared to the CIH + s-EV + sh-NC group (Fig. 5C).

To further understand the metabolic changes, we analyzed the products and enzymes involved in carbohydrate and fatty acid metabolism. The results showed a significant reduction in the FAO-related enzyme carnitine palmitoyltransferase 1b (CPT1b) and its intermediates in the CIH + s-EV group compared to the NO + s-EV group (Fig. 5D). Similarly, intermediate products and enzymes of the TCA cycle, such as succinate dehydrogenase complex subunit B (SDHB) and citrate synthase (CS), were significantly reduced in the CIH + s-EV group (Fig. 5E). In contrast, glycolysis-related intermediates and the enzyme lactate dehydrogenase A (LDHA) were elevated in the CIH + s-EV group compared to the NO + s-EV group

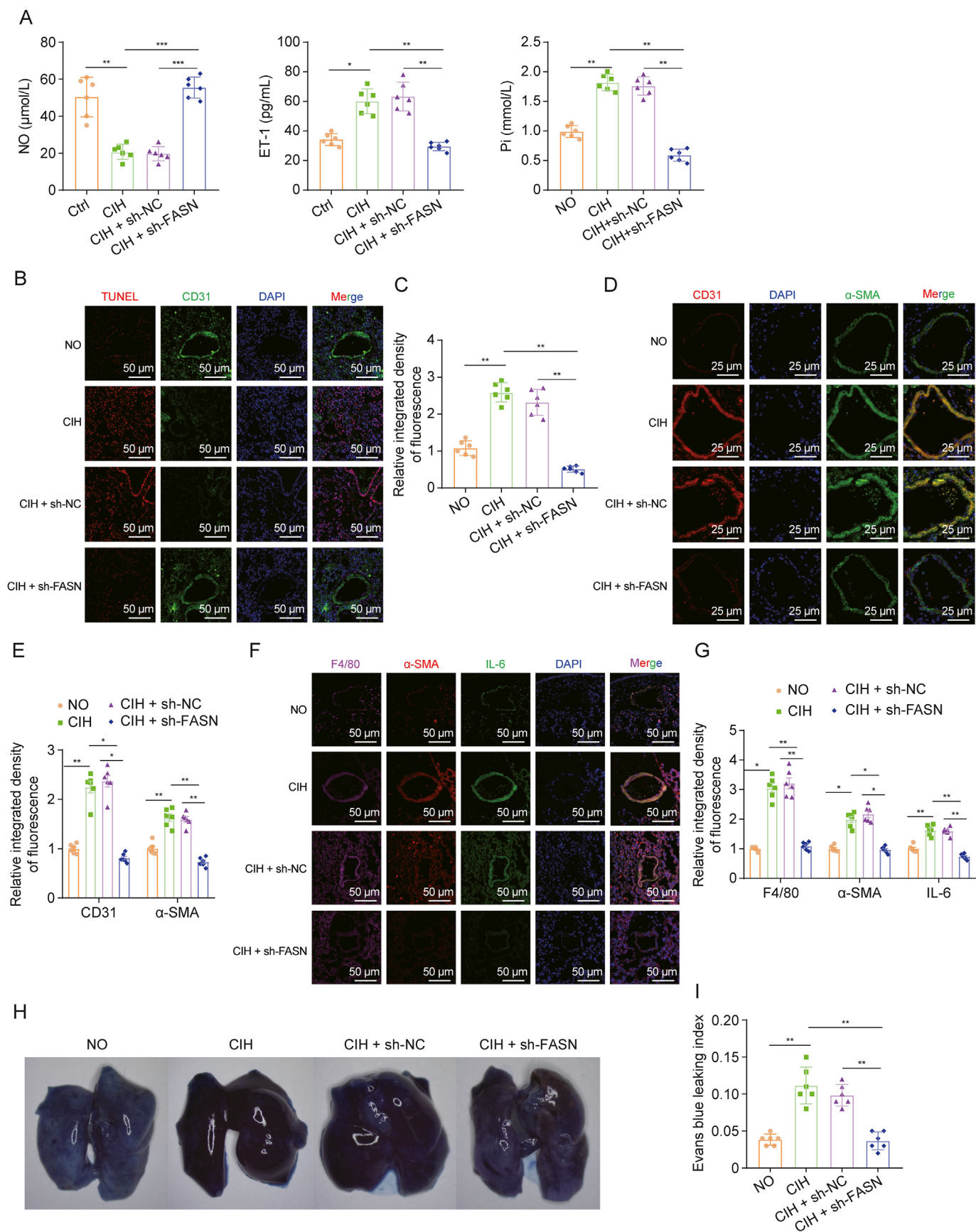


**Fig. 7.** The intervention of fatty acid synthase (FASN) improves endothelial permeability by inhibiting apoptosis of endothelial cells. (A) enzyme-linked immunosorbent assay (ELISA) assay was performed to measure the levels of endothelial function markers normoxia (NO), inorganic phosphate (Pi), and endothelin-1 (ET-1) in the peripheral blood of

(Fig. 5F). However, FAO was restored in the CIH + s-EV-sh-FASN group compared to the CIH + s-EV + sh-NC group (Fig. 5G), and the CIH + s-EV-sh-FASN group also reestablished normal TCA activity, as seen by the restoration of SDHB and CS levels (Fig. 5H). In contrast, silencing FASN downregulated glycolysis in the CIH + s-EV-sh-FASN group compared to the CIH + s-EV + sh-NC group (Figs. 5G and H). The FAO and TCA cycle related to fatty acid consumption were significantly decreased in energy metabolism. Oil red O staining revealed a significant increase in lipid droplets in cells of the CIH + s-EV group compared to the NO + s-EV group. Silencing FASN in the CIH + s-EV-sh-FASN group restored the lipid droplets to normal levels (Fig. 5I).

In summary, we found that FASN-mediated mitochondrial dysfunction positively regulates the glycolytic process in endothelial cells and negatively regulates mitochondrial oxidation processes associated with fatty acid consumption, leading to lipid accumulation within the cells. This lipid accumulation further impacts the progression of vascular-related diseases.

### 3.7. FASN involvement in vascular disease progression through regulation of endothelial cell adhesion and inflammatory factor expression

Previous studies have indicated that the recruitment and accumulation of monocytes, as well as their migration across the endothelium, are critical steps in various vascular diseases [42]. Recent research has found significant changes in the adhesive molecule VCAM-1 in endothelial cells subjected to CIH treatment. As an important adhesion molecule, VCAM-1 can promote the aggregation of inflammatory cells to the vascular wall, thereby exacerbating local inflammatory reactions [43].

Initially, we examined the effect of EV-mediated interventions on FASN expression in THP-1 cells. We found a significant upregulation of FASN following CIH treatment and EV-mediated intervention compared to the NO and EV-treated group. In contrast, FASN expression was significantly lower in the CIH + s-EV + sh-FASN group compared to the CIH, EV, and sh-NC group (Figs. 6A and B). Next, we investigated the adhesion of THP-1 cells to MAECs across different treatment groups. The results showed a significant increase in THP-1 cell adhesion to MAECs following EV-mediated interventions after CIH treatment. However, adhesion was markedly reduced in the CIH + s-EV-sh-FASN group compared to the CIH, EV, and sh-NC groups (Figs. 6C and D).

We used RT-qPCR and Western blot to measure VCAM-1 expression in MAECs co-cultured with THP-1 cells for 24 h under various conditions. The data revealed a significant increase in VCAM-1 expression after EV-mediated interventions following CIH treatment, compared to the NO and EV group. However, this effect was reversed in the CIH + s-EV-sh-FASN group compared to the CIH, EV, and sh-NC groups (Figs. 6E and F). Immunofluorescence analysis revealed changes in endothelial cell adhesion molecules after EV-mediated interventions following CIH treatment. In the NO and EV-treated group, the cell-cell connection network, including VE-cadherin, platelet endothelial cell adhesion molecule-1 (PECAM-1), and zonula occludens-1 (ZO-1), remained intact. However, CIH-treated cells showed disrupted connections and

intercellular gaps. The CIH + s-EV-sh-FASN group displayed a well-organized cellular network, similar to the NO and EV group (Fig. 6G). The disruption of the cell's molecular connection network led to the formation of intercellular gaps, reduced tightness, and increased permeability.

We also evaluated the expression of inflammatory factors in cell lysates. A significant increase in inflammatory factor expression was observed after EV-mediated interventions following CIH treatment, compared to the NO and EV group. However, the CIH + s-EV-sh-FASN group showed a reduction in inflammatory factors compared to the CIH and sh-NC groups (Figs. 6H and J). Our previous studies indicated a significant increase in ROS levels within cells following CIH treatment, suggesting that the notable upregulation of inflammatory factors might be attributed to the elevated intracellular ROS levels.

In summary, our research suggests that FASN promotes macrophage adhesion to endothelial cells, thereby recruiting inflammatory factors within them.

### 3.8. Animal experiments confirmed that FASN induces endothelial permeability enhancement and inflammatory factor expression

In a series of cell experiments, we demonstrated that FASN-induced ROS increases mediate mitochondrial dysfunction, enhancing endothelial cell apoptosis. This process alters endothelial permeability and the expression of adhesion molecules, significantly elevating inflammatory factor levels. To further validate these findings, we conducted animal experiments.

We analyzed the indicators in serum reflecting endothelial function such as Pi, NO, and endothelin-1 (ET-1). The results showed a significant increase in serum Pi and ET-1 levels in the CIH group, while NO levels were significantly reduced. After silencing the FASN gene, serum Pi and ET-1 levels decreased significantly, while NO levels increased (Fig. 7A). To evaluate endothelial function within blood vessels, we performed TUNEL/CD31 double-staining (CD31 as an endothelial cell marker). The CIH group displayed a significant increase in apoptotic cells compared to the control group, whereas silencing FASN significantly reduced the number of positive apoptotic cells (Figs. 7B and C), confirming the role of FASN in regulating endothelial cell apoptosis.

By marking endothelial cell marker CD31 and vascular smooth muscle marker  $\alpha$ -SMA-positive cells, we evaluated the integrity of the vascular cross-section. It was observed that CD31/ $\alpha$ -SMA-positive cells significantly increased in the CIH group mice, while they decreased significantly after silencing FASN (Figs. 7D and E).

To examine the effect of macrophage-recruited inflammatory factors on endothelial cells, we analyzed the expression of F4/80,  $\alpha$ -SMA, and interleukin-6 (IL-6) in vessel cross-sections. In the CIH group, there was a marked accumulation of macrophages and elevated inflammatory factor levels, which decreased significantly after silencing FASN (Figs. 7F and G).

Evan's blue staining of the lungs confirmed that the lungs of CIH group mice exhibited more blue dye leakage than the control group, indicating enhanced endothelial permeability. However, after silencing FASN, the Evans blue leakage in the lungs of mice decreased, suggesting the restoration of endothelial permeability (Figs. 7H and I).

mice. (B, C) Terminal deoxynucleotidyl transferase-mediated dUTP nick end labeling (TUNEL)/ cluster of differentiation 31 (CD31) double immunofluorescence staining in the dysfunctional area (B) and the statistical data (C). (D, E) Estimation of endothelial integrity in vascular cross-sections based on CD31 fluorescence intensity, with lower intensity indicating greater endothelial injury (D) and the statistical data (E). (F, G) Triple immunofluorescence staining of F4/80/ $\alpha$ -smooth muscle actin ( $\alpha$ -SMA)/ interleukin-6 (IL-6) to observe endothelial cells in vascular cross-sections (F) and the statistical data (G). (H, I) Lung blue dye perfusion images (H) and Evans blue leakage index (I). Tissue samples shown in each group represent typical samples, reflecting the overall trend. Each group consisted of 6 mice, and data are presented as mean  $\pm$  standard deviation (SD). \* $P < 0.05$  indicates a significant difference, \*\* $P < 0.01$  indicates a highly significant difference, and \*\*\* $P < 0.001$  indicates a very significant difference. NO: normoxia; Ctrl: control; sh-NC: control shRNA; sh-FASN: FASN-targeting shRNA; CIH: chronic intermittent hypoxia; DAPI: 4',6-diamidino-2-phenylindole.

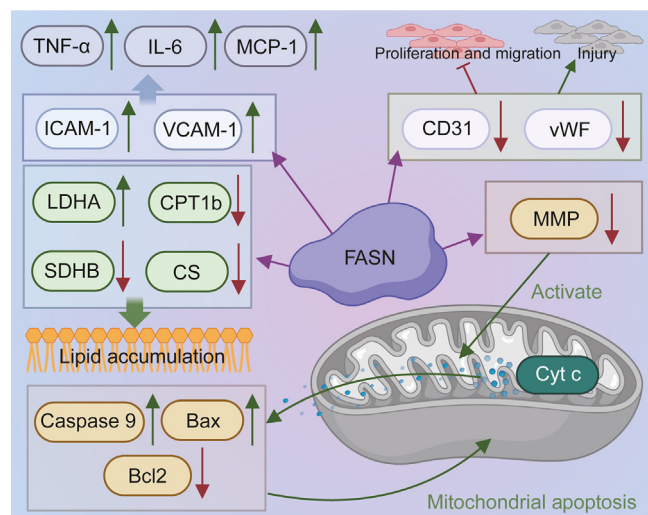


**Fig. 8.** Mechanism of endothelial dysfunction induced by high expression of fatty acid synthase (FASN) in serum-derived extracellular vesicles (s-EVs) from obstructive sleep apnea hypopnea syndrome (OSAHS) patients under intermittent hypoxia conditions. TNF- $\alpha$ : tumor necrosis factor  $\alpha$ ; IL-6: interleukin 6; MCP-1: monocyte chemoattractant protein 1; ICAM-1: intercellular cell adhesion molecule 1; VCAM-1: vascular cell adhesion molecule 1; LDHA: lactate dehydrogenase A; CPT1b: carnitine palmitoyl-transferase 1b; SDHB: succinate dehydrogenase subunit B; CS: citrate synthase; CD31: cluster of differentiation 31; vWF: von Willebrand factor; MMP: matrix metalloproteinase; Cyt-c: cytochrome c; Bax: Bcl-2-associated X protein; Bcl2: B-cell lymphoma 2 (Created by Biorender).

In conclusion, our study results indicate that FASN can induce endothelial cell apoptosis, increase endothelial permeability, and lead to endothelial function disorders. The recruitment of inflammatory factors further exacerbates endothelial function disorders.

#### 4. Discussion

Previous studies have confirmed the link between obstructive OSAHS and endothelial dysfunction [4,5,44]. Prolonged intermittent hypoxia and sleep fragmentation, common in OSAHS patients, can easily trigger the onset and progression of cardiovascular diseases. Our study introduces a novel mechanism of endothelial dysfunction by highlighting the role of FASN-enriched EVs. By analyzing EVs in the serum of OSAHS patients, we found that FASN in EVs may play a crucial role in OSAHS-induced endothelial dysfunction.

Our research stands out for its innovative approach compared to previous studies. First, we employed advanced proteomics and metabolomics techniques, analyzing the protein and metabolite composition of EVs in the serum of OSAHS patients using liquid chromatography-tandem mass spectrometry (LC-MS/MS), liquid chromatography-mass spectrometry (LC-MS), and gas chromatography-mass spectrometry (GC-MS). This comprehensive analysis allowed for a deeper understanding of the mechanisms linking OSAHS to endothelial dysfunction.

Through proteomics and metabolomics analysis, we identified FASN as a significant player in OSAHS-induced endothelial dysfunction. The analysis of DEPs and metabolites revealed significant enrichment of pathways related to EV release, carbohydrate metabolism, fatty acid metabolism, and apoptosis in EVs from OSAHS patients. The enrichment of FASN further supported our hypothesis.

In contrast to previous studies, our research innovatively linked EVs and FASN to endothelial dysfunction in OSAHS patients. This link was further validated by proteomics and metabolomics results.

Through *in vitro* cell experiments and *in vivo* animal models, we further confirmed the impact of FASN in EVs on endothelial cell function. These results provide a new perspective for further research on the pathogenesis of OSAHS.

Clinical data show that the serum CRP levels in OSAHS patients are significantly elevated and positively correlated with disease severity, indicating the presence of an inflammatory process. Additionally, s-EVs from OSAHS patients are enriched with inflammation-related proteins, which exert damaging effects on endothelial cells, leading to endothelial dysfunction. We further elucidated the molecular interactions between s-EVs from OSAHS patients and endothelial cells through proteomic and metabolomic analyses. Notably, in OSAHS patients, the activation of FASN leads to mitochondrial dysfunction in endothelial cells: the expression of endothelial dysfunction markers ICAM-1 and VCAM-1 is increased, while CD31 and vWF expressions are significantly downregulated, inhibiting endothelial cell proliferation and migration, thereby causing endothelial injury. Moreover, the significant reduction in MMP induces the opening of more mPTPs, triggering the activation of the classical mitochondrial apoptosis pathway (resulting in increased mitochondrial ROS production and the release of the pro-apoptotic factor Cyt-c from the mitochondria into the cytoplasm). This upregulates pro-apoptotic proteins caspase 9 and Bax, while downregulating the anti-apoptotic factor Bcl2, indicating the activation of mitochondrial apoptosis. Furthermore, FASN activation promotes the upregulation of the glycolytic pathway and suppresses the FAO pathway. Specifically, the intermediate metabolites and enzymes of the FAO process, such as CPT1b, are significantly reduced, and the intermediate metabolites and related enzymes of the TCA cycle, including SDHB and CS, are also significantly reduced. Conversely, the expression of intermediate metabolites and the enzyme LDHA in the glycolysis pathway is significantly increased, resulting in lipid accumulation in endothelial cells. These changes may help explain the occurrence of endothelial dysfunction. In addition, the study reveals that under CIH conditions, activated FASN increases the migration of macrophages and their adhesion to endothelial cells by regulating adhesion molecules like VCAM-1, thereby amplifying the local inflammatory response, significantly increasing the expression of inflammatory factors TNF- $\alpha$ , IL-6, and MCP-1 (Fig. 8).

Our study's findings have significant implications for scientific research and potential clinical applications. Uncovering the novel mechanism of FASN-enriched EVs in OSAHS-related endothelial dysfunction enhances our understanding of OSAHS's pathophysiological processes. Moreover, this discovery opens new avenues for developing therapeutic strategies. Targeting FASN or EVs could provide a novel approach to treating OSAHS.

Despite the important progress made, our study has some limitations. The sample size was relatively small, and larger-scale studies are needed to further validate our findings. Additionally, while our results underscore the role of FASN in OSAHS-related endothelial dysfunction, more research is required to precisely target and regulate FASN. Future studies will focus on elucidating the mechanisms of EV interaction with endothelial function and identifying targeted interventions to improve the health of OSAHS patients.

#### 5. Conclusion

We selected serum from clinical OSAHS patients and found significantly elevated CRP levels. To explore the effect of s-EVs on pulmonary endothelial injury, we isolated s-EVs from OSAHS patients and non-OSAHS groups using ultracentrifugation. The combined proteomics and metabolomics analysis revealed that FASN is a key protein involved in lipid metabolism in OSAHS patient-

derived s-EVs. PKH26-labeled s-EVs from OSAHS patients and control groups were injected into mice cultured in NO and CIH conditions, respectively. We found that s-EVs from OSAHS patients induced pulmonary endothelial dysfunction. Further studies using this mouse model revealed that FASN in CIH-derived s-EVs inhibited endothelial cell proliferation and migration, leading to endothelial injury. FASN-mediated mitochondrial dysfunction caused endothelial cell apoptosis and increased permeability. FASN positively regulated the glycolytic pathway in endothelial cells and negatively regulated mitochondrial FAO, leading to lipid accumulation. FASN promoted macrophage adhesion to endothelial cells, recruiting inflammatory factors into the endothelial cells. Follow-up animal experiments confirmed that FASN induces endothelial cell apoptosis, increases permeability, and causes endothelial dysfunction. The recruitment of inflammatory factors further exacerbated endothelial dysfunction.

### CRedit authorship contribution statement

**Yuan Tian:** Conceptualization. **Dan Zhang:** Conceptualization, Data curation, Formal analysis, Investigation, Methodology, Software, Writing – review & editing. **Huaian Yang:** Conceptualization. **Xiaoli Zhang:** Conceptualization, Data curation, Formal analysis, Software, Validation, Writing – review & editing. **Shengqun Xu:** Conceptualization.

### Ethical statement

This study was approved by the Clinical Ethics Committee of Shengjing Hospital of China Medical University.

All animal experiments were approved by the Animal Ethics Committee of Shengjing Hospital of China Medical University (2024PS160K).

### Declaration of competing interest

The authors declare that there are no conflicts of interest.

### Appendix A. Supplementary data

Supplementary data to this article can be found online at <https://doi.org/10.1016/j.jpha.2025.101251>.

### References

- X. Yang, X. Niu, Y. Xiao, et al., MiRNA expression profiles in healthy OSAHS and OSAHS with arterial hypertension: Potential diagnostic and early warning markers, *Respir. Res.* 19 (2018), 194.
- C.H.G. Uchôa, R.P. Pedrosa, S. Javaheri, et al., OSA and prognosis after acute cardiogenic pulmonary edema: The OSA-CARE study, *Chest* 152 (2017) 1230–1238.
- S.O. Serin, G. Karaoren, A.M. Esquinas, OSA and recurrent VTE: Causality or cause? *Chest* 151 (2017) 514–515.
- F. Yuan, S. Zhang, X. Liu, et al., Correlation between obstructive sleep apnea hypopnea syndrome and hypertension: A systematic review and meta-analysis, *Ann. Palliat. Med.* 10 (2021) 12251–12261.
- H. Li, L. Chen, X. Wu, et al., The effects of obstructive sleep apnea-hypopnea syndrome (OSAHS) on learn and memory function of 6–12 years old children, *Int. J. Pediatr. Otorhinolaryngol.* 159 (2022), 111194.
- L. Ma, F. Song, Obstructive sleep apnea-hypopnea syndrome complicated with idiopathic intracranial hypertension: A case report, *Ann. Palliat. Med.* 11 (2022) 3833–3839.
- S. Javaheri, R. Germany, Sleep and breathing disorders in heart failure, *Handb. Clin. Neurol.* 189 (2022) 295–307.
- P. Cai, Y. Zheng, Y. Zhou, et al., Research progress on the role of exosomes in obstructive sleep apnea-hypopnea syndrome-related atherosclerosis, *Sleep Med. Rev.* 66 (2022), 101696.
- L. Li, Y. Yang, H. Zhang, et al., Salidroside ameliorated intermittent hypoxia-aggravated endothelial barrier disruption and atherosclerosis via the cAMP/PKA/RhoA signaling pathway, *Front. Pharmacol.* 12 (2021), 723922.
- J. Zou, W. Yang, W. Cui, et al., Therapeutic potential and mechanisms of mesenchymal stem cell-derived exosomes as bioactive materials in tendon–bone healing, *J. Nanobiotechnol.* 21 (2023), 14.
- G. van Niel, D.R.F. Carter, A. Clayton, et al., Challenges and directions in studying cell–cell communication by extracellular vesicles, *Nat. Rev. Mol. Cell Biol.* 23 (2022) 369–382.
- R. Kalluri, K.M. McAndrews, The role of extracellular vesicles in cancer, *Cell* 186 (2023) 1610–1626.
- H. Zhang, F. Yang, Y. Guo, et al., The contribution of chronic intermittent hypoxia to OSAHS: From the perspective of serum extracellular microvesicle proteins, *Metabolism* 85 (2018) 97–108.
- R. Bhattacharjee, A. Khalifa, A.A. Khalifa, et al., Exosomal cargo properties, endothelial function and treatment of obesity hypoventilation syndrome: A proof of concept study, *J. Clin. Sleep Med.* 14 (2018) 797–807.
- A. Khalifa, D. Gozal, L. Kheirandish-Gozal, Plasma extracellular vesicles in children with OSA disrupt blood–brain barrier integrity and endothelial cell wound healing in vitro, *Int. J. Mol. Sci.* 20 (2019), 6233.
- D. Sanz-Rubio, A. Khalifa, Z. Qiao, et al., Cell-selective altered cargo properties of extracellular vesicles following in vitro exposures to intermittent hypoxia, *Int. J. Mol. Sci.* 22 (2021), 5604.
- K. Cao, T. Zhang, Z. Li, et al., Glycolysis and de novo fatty acid synthesis cooperatively regulate pathological vascular smooth muscle cell phenotypic switching and neointimal hyperplasia, *J. Pathol.* 259 (2023) 388–401.
- M. Aregger, K.A. Lawson, M. Billmann, et al., Systematic mapping of genetic interactions for de novo fatty acid synthesis identifies C12orf49 as a regulator of lipid metabolism, *Nat. Metab.* 2 (2020) 499–513.
- Y. Chen, Z. Wang, X. Xian, et al., Eukaryotic initiation factor 6 repression mitigates atherosclerosis progression by inhibiting macrophages expressing Fasn, *IUBMB Life* 75 (2023) 440–452.
- W. Dai, Z. Wang, G. Wang, et al., FASN deficiency induces a cytosol-to-mitochondria citrate flux to mitigate detachment-induced oxidative stress, *Cell Rep.* 42 (2023), 112971.
- Y. Liu, L. Liu, Y. Jia, et al., Role of microRNA-15a-5p in the atherosclerotic inflammatory response and arterial injury improvement of diabetic by targeting FASN, *Biosci. Rep.* 39 (2019), BSR20181852.
- C. Wu, Z. Shen, Y. Lu, et al., p53 promotes ferroptosis in macrophages treated with Fe3O4 nanoparticles, *ACS Appl. Mater. Interfaces* 14 (2022) 42791–42803.
- A. Luo, X. Zhou, X. Shi, et al., Exosome-derived miR-339-5p mediates radio-sensitivity by targeting Cdc25A in locally advanced esophageal squamous cell carcinoma, *Oncogene* 38 (2019) 4990–5006.
- Y. Su, C. Quan, X. Li, et al., Mutual promotion of apoptosis and autophagy in prepubertal rat testes induced by joint exposure of bisphenol A and non-ylphenol, *Environ. Pollut.* 243 (2018) 693–702.
- K.X. Zhou, S. Huang, L.P. Hu, et al., Increased nuclear transporter KPNA2 contributes to tumor immune evasion by enhancing PD-L1 expression in PDAC, *J. Immunol Res* 2021 (2021), 6694392.
- Y. Zhang, C. Ning, H. Zhou, et al., Interleukin-1 $\beta$ , interleukin-6, and interleukin-17A as indicators reflecting clinical response to celecoxib in ankylosing spondylitis patients, *Ir. J. Med. Sci.* 190 (2021) 631–638.
- G. Zhu, Z. Cheng, Y. Huang, et al., MyD88 mediates colorectal cancer cell proliferation, migration and invasion via NF- $\kappa$ B/AP-1 signaling pathway, *Int. J. Mol. Med.* 45 (2020) 131–140.
- L. Guo, Y. Wang, S. Li, et al., Elevated fibroblast growth factor 23 impairs endothelial function through the NF- $\kappa$ B signaling pathway, *J. Atherosclerosis Thromb.* 30 (2023) 138–149.
- Y. Guo, X. Jia, Y. Cui, et al., Sirt3-mediated mitophagy regulates AGEs-induced BMSCs senescence and senile osteoporosis, *Redox Biol.* 41 (2021), 101915.
- Z. Wu, H. Huang, Q. Han, et al., SENP7 senses oxidative stress to sustain metabolic fitness and antitumor functions of CD8+ T cells, *J. Clin. Investig.* 132 (2022), e155224.
- R.J. Stark, S.R. Koch, C.L. Stothers, et al., Loss of Sirtuin 1 (SIRT1) potentiates endothelial dysfunction via impaired glycolysis during infectious challenge, *Clin. Transl. Med.* 12 (2022), e1054.
- W. Zhao, L. Ma, C. Cai, et al., Caffeine inhibits NLRP3 inflammasome activation by suppressing MAPK/NF- $\kappa$ B and A2aR signaling in LPS-induced THP-1 macrophages, *Int. J. Biol. Sci.* 15 (2019) 1571–1581.
- Z. Wu, G. Zhao, L. Peng, et al., Protein kinase C beta mediates CD40 ligand-induced adhesion of monocytes to endothelial cells, *PLoS One* 8 (2013), e72593.
- J. Shen, D. Yang, X. Zhou, et al., Role of autophagy in zinc oxide nanoparticles-induced apoptosis of mouse LEYDIG cells, *Int. J. Mol. Sci.* 20 (2019), 4042.
- Q. Zhang, J. Li, K. Jiang, et al., CDK4/6 inhibition promotes immune infiltration in ovarian cancer and synergizes with PD-1 blockade in a B cell-dependent manner, *Theranostics* 10 (2020) 10619–10633.
- V. Schirmmacher, Mitochondria at work: New insights into regulation and dysregulation of cellular energy supply and metabolism, *Biomedicines* 8 (2020), 526.
- Z. Guo, D. Fan, F. Liu, et al., NEU1 regulates mitochondrial energy metabolism and oxidative stress post-myocardial infarction in mice via the SIRT1/PGC-1 alpha axis, *Front. Cardiovasc. Med.* 9 (2022), 821317.
- Q. Lei, J. Tan, S. Yi, et al., Mitochondrial acid 5 activates the MAPK–ERK–Yap signaling pathways to protect mouse microglial BV-2 cells against TNF $\alpha$ -induced apoptosis via increased Bnip3-related mitophagy, *Cell. Mol. Biol. Lett.* 23 (2018), 14.

- [39] Y. Wang, Y. Yuan, X. Wang, et al., Tiliarin post-conditioning attenuates myocardial ischemia/reperfusion injury via mitochondrial protection and inhibition of apoptosis, *Med. Sci. Monit.* 23 (2017) 4490–4499.
- [40] A. Ibrahim, N. Yucel, B. Kim, et al., Local mitochondrial ATP production regulates endothelial fatty acid uptake and transport, *Cell Metab.* 32 (2020) 309–319.e7.
- [41] S. Schoors, U. Bruning, R. Missiaen, et al., Fatty acid carbon is essential for dNTP synthesis in endothelial cells, *Nature* 520 (2015) 192–197.
- [42] K.W. Kim, S. Ivanov, J.W. Williams, Monocyte recruitment, specification, and function in atherosclerosis, *Cells* 10 (2020), 15.
- [43] S. Zhang, B. Xie, L. Wang, et al., Macrophage-mediated vascular permeability via VLA4/VCAM1 pathway dictates ascites development in ovarian cancer, *J. Clin. Investig.* 131 (2021), e140315.
- [44] J. He, X. Li, M. Yu, The correlation of serum/plasma IGF-1 concentrations with obstructive sleep apnea hypopnea syndrome: A meta-analysis and meta-regression, *Front. Endocrinol.* 13 (2022), 922229.